이학박사 학위논문

DNA Assay Based on Nanoparticle-modified 2D Lipid Bilayer Micropattern Platform

2차원 유동적 지지형 지질 이중막 마이크로패턴 나노입자 플랫폼을 이용한 DNA 분석

2017년 8월

서울대학교 대학원

화학부 무기화학

김 근 석

Abstract

DNA Assay Based on Nanoparticle-modified 2D Lipid Bilayer Micropattern Platform

Keunsuk Kim

Department of Chemistry

The Graduate School

Seoul National University

Lipids are a group of naturally occurring molecules that contain hydrocarbon and are soluble in nonpolar solvents, which are including diverse group of organic compounds such as fats, waxes, steroids, glycolipids, and phospholipids. They play an essential role in organisms such as storing energy, signaling, and constructing cell membrane structures. Phospholipids as the dominant lipid molecules in cell membranes, contain hydrophilic head groups and hydrophobic tails, which governs the spontaneous self-assembled bilayer structure. Then, phospholipid bilayer can be used as a fluidic membrane for the dynamic reaction or a cell mimicking model membrane for the biological study. Especially, supported lipid bilayers (SLBs) of phospholipids on solid

glasses can endow the various physical and chemical functionalities of controlling biomolecules reaction, the modification capabilities to incorporate various biomolecules, and the robust platform to monitor the dynamic reactions by optical devices.

DNA, deoxyribonucleic acid, is an essential molecule for organisms to survive and reproduce, which contains genetic codes for inheritance. All the genetic information is encoded by a characteristic sequence of four kinds of bases (i.e. adenine (A), cytosine (C), guanine (G), and thymine (T)) in a DNA strand. Mutation or random change in this DNA sequence by accidental exposure to mutagens or copying errors in DNA replication process, can result in the distortion of inheritance or malfunctioned genetic disorder, which cause genetic diseases or cancers. In the past decades, DNA bioassay has received broad attention due to its potential applications in a diversity of fields, e.g., clinical diagnosis, biomedical engineering, food development, environmental protection, forensic investigation and screening of biowarfare agents. One of main challenges in the development of DNA biosensors is the ultrasensitive, quantifiable, and highly reliable DNA detection without any help of amplification; amplification steps using enzymes, fluorescence dyes, and nanomaterials suffer from the erroneous signals by the amplification of the false signals or background signals, need complexed experimental procedures, and cause the signals to be vulnerable to a variety of environmental factors. To realize such an amplification-free, ultrasensitive DNA detection, an endeavor to discriminate rare true-signals from false-signals is necessary. Here, we employed the plasmonic nanoparticles-tethered fluidic SLB platform.

Plamonic nanoparticles can generate highly strong light scattering signals and a molecular binding-involved distance change between nanoparticles at the several nanometers level can be detected by the plasmonic coupling. Moreover, the 2D fluidic lipid bilayer can concentrate target DNAs and improve the efficiency of binding reactions in a 2D lipid bilayer pattern. Accordingly, we firstly studied the characteristic properties and fundamental behaviors of SLB layer and nanoparticles on SLB layer with various experimental conditions. Next, the optimized conditions for the ultrasensitive DNA sensing were obtained. Furthermore, this platform and methodology can be applied to the discrimination of various point mutated single-nucleotide polymorphism (SNP) sequences.

In chapter 1, we describe recently developed nanomaterial-tethered SLB platform in a formational standpoint. We summarize representative and convenient methods for the formation of supported phospholipid bilayers on planar hydrophilic substrates or micropatterns and linking methods for connecting between nanomaterials and the surface of the bilayer in a synthetic standpoint. We further focus on applications of nanomaterial-tethered SLB in biosensors to detect target molecules with ultrasensitivity and high target specificity.

In chapter 2, we studied ultrasensitive and high-selective DNA bioassay through kinetic analysis of dissociation nanodimers using nanomaterial-tethered SLB platform. Amplification/enzyme-free detection and quantification of DNA at ultra-low concentrations, typically 10s-1,000s of targets in solution, is highly challenging but beneficial by offering a more

straightforward, less contamination-prone, temperature control-free, less expensive, more quantitative and highly selective detection method than amplification/enzyme-based methods such as the polymerase chain reaction (PCR). Here, we developed an ultrasensitive, highly reliable bio-analytical method [the dynamic analysis on whole nanoparticle cumulative binding events (DANCE)] that allows for quantitatively analyzing dynamically associating and dissociating dimers generated by recognition of DNA strands with two-dimensionally mobile, photostable, and dark-field-detectable DNA-modified nanoparticles (NPs) on a lipid bilayer micropattern. Our results show that the amplification/enzyme-free DANCE provides the PCR-like sensitivity with high target specificity and excellent quantification capability for 10s-1,000s of DNA strands in a whole sample.

In chapter 3, we used nanomaterial-tethered SLB biosensor to analyze sensitively mutant position determination of single base mismatched (SBM) DNA sequences. Although the thermodynamic difference among the mutant position-variable SBM sequences is too minuscule to differentiate them, we can measure and analyze the dissociation constants (k_{off}) of various SBM sequences, respectively, which is obtained by counting dissociating nanodimers. As the sequence length is longer, k_{off} value is gradually smaller due to the stability of duplex via multiple Watson-Crick base-pairing; however, the significant reduction of k_{off} value from 6mer to 7mer sequences were exhibited, which seems to be related to the seven contiguous Watson-Crick base pair rule. By comparison of dissociations among 7mer, 13mer and 15mer DNA duplex systems, we also proved the seven contiguous Watson-Crick

base pair rule, even though more than 10mer sequence. Kinetic information of SBM sequences obtained by counting the dissociation events of DNA mediated plasmonic nanodimer, is very sensitive to discriminate mutant point SBM sequences and helpful to understand the mechanism of DNA hybridization dynamics at the single molecular level. Moreover, our research and platform are expected to give much insight into unveiling the dynamic information of various biological reactions among biomaterials such as nucleic acids, proteins, and carbohydrates and the new biological mechanisms in the cellular level.

Contents

List of Figures

Chapter 1

nanolithography (DPN) cantilever array. Right: fluorescence images of multilayered 1,2-dioleoyl-sn glycero-3-phosphocholine (DOPC) structures containing fluorophore-labeled lipids (rhodamine/red and fluorescein/green). (d) Left: schematic illustration of atomic force microscopy (AFM)-based nanoshaving lithography for nanoscale supported lipid bilayer (SLB) formation. Right: epifluorescence images of a nanoshaved bovine serum albumin (BSA) monolayer (top) and SLB lines (bottom). The scale bar is 3 mm. (e) Top: schematic overview of nanoparticle array-embedded SLBs. Middle: from the left, reference SEM image of gold nanoparticle arrays and photoactivated localization microscopy (PALM) image of individual ephrin-mEos-His10 molecules conjugated on the same gold nanoparticle array. The scale bar is 200nm in both cases. The right figure represents comparison of the radial distribution function from the full PALM image (black) and the reference SEM image (red). Bottom: fluorescence recovery after photobleaching (FRAP) on a bilayer of DOPC doped with 0.5% Texas Red-1,2-dihexadecanoyl-sn-glycero-3 phosphoethanolamine (DHPE). ……28

Figure 1.5. Various techniques to tether nanomaterials onto SLBs. Various techniques to tether nanomaterials onto SLBs. (a) Scale illustration of different antibody-adsorbed particles for attachment to fluorescent lipids in a SLB. (b) Biotin DNA-modified gold nanoparticles binding to biotinylated-SLB with streptavidin. (c) CTB (i.e. CTxB)-modified gold nanoparticle with GM1-lipid. The gold nanoparticle is functionalized with streptavidin, and then reacted with a concentration of biotinylated CTB to achieve an average of one

Figure 1.6. (a) Single nanoparticle tracking-based detection on supported lipid bilayer platform and time-lapse dark-field images of lipid-tethered AuNPs on supported lipid bilayer (b) Schematic illustration of dynamic two dimensional confinement of plasmonic nanoparticles on lipid bilayer surface. Two different types of probes (mobile and immobile plasmonic probes) are tethered to a supported lipid bilayer. Target DNA hybridization induces two dimensional cluster formation and plasmonic coupling. Dark-field microscopic images of target DNA hybridization-induced plasmonic nanoparticle clusters. Representative time traces of the scattering intensity for assembly processes of nanoparticle clusters (c) Optokinetically encoded nanoprobe (OK-NP)-tethered supported lipid bilayer (SLB) assay (OK-NLB assay). The miRNA sample is directly injected into a reaction chamber, and NP interactions are monitored with dark-field microscopy (DFM). Six types of OK-NPs are prepared by kinetic [mobile (M) and immobile (I)] and optical [red (R), green (G), and blue (B)] coding methods. OK-NPs are composed of plasmonic nanoparticle core, multiple target capture DNAs, and biotinylated DNA. The NP assembly events between the M-NPs and the I-NPs are mediated by target miRNAs and identified with scattering color changes via plasmonic coupling. The nineplexing strategy using combinatorial assemblies between OK-NPs relies on each assembly mode, which was mediated by 9 different target miRNAs. (d) Graphical illustration of vesicles being tethered

Chapter 2

Chapter 1

Introduction: Nanomaterial-tethered Supported Lipid Bilayers and Their Applications

1.1. Introduction

Cell membranes are comprised of a variety of lipid and functional proteins that provide active platforms which are involved in the conformational change and perform biologically special reaction with the fluidity of cell membrane. Such a dynamic and complex properties renders native cell membranes experimentally uncertain and difficult. And limited methods to precisely estimate physical and chemical specificity of cell membranes makes great demand on a research platform to not only reduce the complexity and uncertainty but also offer many of biological key features including lateral fluidity and compatibility with membrane factors. In this respect, supported lipid bilayers (SLBs), self-assembled lipid bilayers on solid substrates, are a model membrane platform that uses powerful artificial cell membranes in a synthetically controllable manner, while recapitulating membrane key functions. During the past two decades, SLBs have been decorated with a variety of membrane-associated molecules and coupled with microfluidic and microarray techniques.[1, 2] These enable advances of SLB-based membrane-mimicking systems for sensing membrane reactions, studying intercellular signaling and separation of membrane species.[3-6]

Also, nanomaterials have been of great fascinative because their shape, dimensions and composition-dependent properties are compatible with biological systems, which allows for a great chance to investigate dynamic membrane and biological phenomena at the sub-cellular level with high sensitivity. Recent progressive advances in synthetic and fabrication methods

for functional nanomaterials including metallic nanoparticles, semiconductor nanoparticles, metal oxide nanoparticles, nanotube/wire, nanopore modified by biomolecules, genes and proteins, with fine controllability boost development of new methodologies to extract thermodynamic information between complex biological molecules.

Rational fabrication of lipid-nanomaterials hybrids on flat support allows showing two dimensional (2D)-dynamic motion of nanomaterials on artificial cell membrane environments.[7] This platform can offer the biomolecules dynamically to interact on 2D SLBs for understanding association and dissociation of biomolecules, nucleic acids or antibodies and antigens. In addition, the hybrid system can expand the utility of nanomaterial-based biosensor to detect molecular reactions occurring on the membrane surface by displaying membrane receptors of interest in active sensing areas. The lipid bilayer also promotes devising biosensors with new working principles based on their unique properties such as high electrical resistance and lateral fluidity. Thus, the hybrid of the lipid bilayers and the nanomaterials provides exciting new opportunities for cell membrane study and biosensing application which is unprecedented in terms of sensitivity and spatial resolution.

In this chapter, we describe convenient methods for the formation of supported phospholipid bilayers on planar hydrophilic substrates or micropatterns and linking methods for connecting between a nanomaterials and the surface of the bilayer in a synthetic standpoint. We further focus on application of nanomaterial-tethered SLB in biosensors to detect target

molecules with ultrasensitivity and high target specificity.

1.2. Formation of Nanomaterial-tethered Supported Lipid Bilayer (SLB)

This part will discuss three general methods for the formation of supported lipid bilayer on planar supports or micorpatterns. For this case, lipid molecules should be adsorbed and then rearranged to be self-assembled on the 2D surface. Also, tethering techniques for mobile bilayer attachment and mobility control are studied by the descriptions and the results of nanomaterial-tethered lipid membranes in terms of formation kinetics, stability, gel-fluid coexistence regime and dynamics of lipid molecules. Therefore, selecting suitable synthetic methods and understanding such interactions between membranes and nanomaterials allow one to rationally design and synthesize the nano/bio hybrid materials that present a high-performance in sensing applications.

1.2.1. The Formation of SLB

Solid supported lipid bilayers furnish a fine model system for understanding the surface chemistry of the cell. Moreover, they are accessible to a wide variety of analytical techniques. In solid supported systems, the fluidity of lipid bilayers is maintained by a 10–20 Å layer of trapped water between the substrate and the bilayer.[8, 9] A schematic diagram of a supported lipid bilayer (SLB) is shown in Figure 1.1. Various substrates capable of SLB are somewhat limited. In order to achieve a high quality of membrane (i.e. little or no defects and high lipid mobility), the surface should be hydrophilic, smooth, and clean. The best substrates are fused silica[8, 10], borosilicate glass[8,

[11], mica[12, 13], and oxidized silicon[8]. Attempts have been made to underlie supported bilayers on the substrates of TiO2 and SrTiO2 as well as on thin films of SiO2 on LiNbO3 crystals.[14-16] Thin films can be used as solid supports as observed with TiO2[17-19], indium-tin-oxide[20, 21], gold[22, 23], silver[24], and platinum[25]. There are three universal and conventional methods for the formation of supported lipid bilayers on 2D supports for biosensor applications.

The first method involves the transfer of a lower leaflet of lipids from the air–water interface by the Langmuir–Blodgett technique (Figure 1.2a).[2] This is followed by the transference of an upper leaflet by the Langmuir–Schaefer procedure, which involves horizontally dipping the substrate to fabricate the second layer.[8] A second approach of supported lipid bilayer formation is the adsorption and fusion or rupture of vesicles from an aqueous suspension to the substrate surface (Figure 1.2b).[2, 26, 27] Also, a integration of the two methodologies can be used by first transferring a monolayer via the Langmuir–Blodgett technique followed by vesicle fusion to create the upper layer (Figure 1.2c).[2, 28]

Each of the three SLB methods has its particular advantages and disadvantages. The transference of amphiphilic molecules from the air–water interface to a 2D solid substrate dates back to the 1920s.[29] An outstanding review of this topic is discovered.[30] Tamm and McConnell were the first to apply this technology to form supported lipid bilayers by sequential monolayer move onto quartz, glass, and oxidized silicon substrates.[8] This approach is useful for the preparation of asymmetric bilayers[19]; however, it is

hard to incorporate transmembrane proteins into the lipid bilayer with this technique because prior to transfer portions of the proteins within the monolayer are exposed to air and can become irreversibly denatured.[28] The adsorption and fusion or rupture of 100 ~ 200 nm unilaminar vesicles (SUVs) in size is one of the easiest and most versatile means for forming solid supported lipid bilayers (Figure 1.2b). SUVs can be prepared by a variety of methods. The simplest is employed by the extrusion of multilaminar vesicles through porous polycarbonate membranes at high pressure.[31-34] Another method is the sonication and ultracentrifugation of aqueous lipid suspensions.[35] The combination of transmembrane proteins into SUVs requires a milder process such as detergent removal via dialysis.[36, 37] Factors affecting the adsorption and fusion or rupture of SUVs to solid supports is composed of the vesicle composition, size, surface charge, surface roughness, surface cleanliness, solution pH, ionic strength, and the osmotic pressure of the vesicles.[17, 38] The first step in the process begins with the adsorption of SUVs from the bulk solution onto the 2D substrate (Figure 1.3). In the early stages, SUVs may fuse with one another or rupture.[38] The vesicles then rupture and fuse to the substrate forming 2D supported bilayers in a process that depends upon the chemistry of the individual lipids.[39] The step of the adsorption can be enhanced by the existence of divalent cations such as Ca^{2+} and Mg^{2+}.[19] Fusion of vesicles to the substrate can also be accelerated by heating[21], creating an osmotic gradient across the vesicle membrane[17], and by the addition of fusogenic agents such as polyethylene glycol.[40]

Although the exact mechanism of bilayer formation from the adsorption

and fusion or rupture of SUVs is not perfectly studied, mathematical modeling of the process has shown good agreement with experimental results.[2] A combination of Langmuir–Blodgett monolayer transfer and vesicle fusion can also be employed to prepare 2D supported lipid bilayers.[28] Third method mixes the fusion of SUVs to a predeposited monolayer of phospholipid. This approach is highly efficient for the creation of asymmetric bilayers[41] and for the combination of transmembrane proteins on 2D supported lipid bilayers.[28] It is well organized that phospholipid membranes are held in place above a solid oxide support by an integration of van der Waals, electrostatic, hydration and steric forces.[11] For example, in an egg phosphatidylcholine (egg-PC) bilayer supported on a 2D glass substrate, the underlying water layer effectively lubricates the lipids, which allows them to freely move with a lateral diffusion constant of approximately 1–4 μm2/s.[42] Furthermore, it has been observed that negatively charged vesicles are difficult to fuse on glass substrates at basic pH values and low ionic strengths.[11] Uncharged vesicles made from zwitterionic lipids, however, appear to fuse more easily to the surface of Au substrates presenting a charged monolayer rather than to neutral ones.[43]

1.2.2 Micropatterning Fluid Lipid Bilayers on 2D Substrates

Lipid bilayers are selectively assembled and show fluidity on the surface of specific substrates, typically silica. The any of the materials that prevent formation of lipid bilayers or spreading of them over the surface of substrates can be utilized as a diffusion barrier. Incubation of SUVs with substrates

patterned with barriers consisted of metals, polymers and proteins leads to formation of spatial patterns of lipid membranes to which the mobility of molecules is limited.[4, 44, 45] Technological advancements in pattering in terms of variety of materials and spatial resolution offer great opportunities to fabricate micropatterned mobile surface which modulates fluidity of membrane species to confined or hindered diffusion in micrometer dimensions.

Photolithography, optical lithography or UV lithography, is used to fabricate pattern on parts of a thin film or the bulk of a substrate. It uses light to transfer a geometric pattern from a photomask to a light-sensitive photoresistor (PR) on a substrate (Figure 1.4a).[46, 47] The PR exposured by light causes a chemical change that allows that to be removed by special developer. A subsequent lift-off process provides micropatterned-substrates. In 1997, Groves et al. developed a patterning surface with solid supported lipid bilayers.[44] The patterned array is the patterning of photoresist on fused quartz waters by means of standard photolithographic techniques. After creating a lithographically patterned array, fluorescently labeled lipid bilayers were formed onto the substrate between the barriers by the method of vesicle fusion. Also, SLBs were observed to diffuse freely within each membrane corral but were confined by the micropatterned barriers.

Electron-beam lithography has been generally employed to make Cr micropatterns by which lipid bilayers are totally disrupted, and thus they can provide passive barricades to lipid lateral diffusion (Figure 1.4b).[48] Lift-off process with electron beam lithography-generated resist patterns typically

produces about a few nanometer-high and micrometer-wide Cr barriers. This is utilized for engineering spatial organization of cell membrane receptors by living cell interfacing. However, this method can only range from a few nanometers to several micrometers in an area and inevitable exposure of the substrate to high vacuum environment constrains from using this method by direct and successive multi-compositional patterning of biomolecules.

Dip-pen nanolithography (DPN) is a scanning probe-based lithographic technique that is suitable method for patterning by directly delivering ink molecules from the tip of an atomic force microscope to an underlying substrate.[49] A parallel DPN tip has been introduced to create multiplexed pattering of functional molecules and high throughput molecular printing.[50] Poly(diallydimethylammonium chloride) (PDAC) were used as an inking molecule of DPN to provide diffusion barriers and sites for bio-functionalization in SLBs.[51] After SLB formation, resulting PDAC patterns provide a template for protein adsorption and confine lipid diffusion in patterns. In some cases, disjointed lines of PDAC were formed and such structure can take advantage of restricted diffusion to mimic cells and to study non-Brownian diffusion behavior of membrane bound molecules. Phospholipids, major constituents of cell membranes, were directly transferred and formed in patterned fluid lipid films by DPN.[52] Under the adequate relative humidity and scan speed, thickness of lipid deposited can be controlled to that of a single bilayer and lateral resolution is decreased to sub-100 nm. An ability of massively parallel and direct transfer of multicomponent lipids and lipophilic materials to the solid surface on multiple

length scales enables precise mimicking of heterogeneous micro and nanodomains of native cell membranes known as lipid rafts (Figure 1.4c).[53]

An AFM tip can locally carve in pre-existing thin films on a solid supports rather than deliver ink molecules to be patterned, which is so-called nanoshaving lithography (Figure 1.4d).[54] When a shaved region is back filled with a SLB composed of 1-palmitoyl-2-oleoyl-sn-glycero-3-phosphocholine (POPC), lipid membranes selectively cover this area with the narrowest line width of 50 nm.

Nanoarrays of selective protein modification sites in SLBs were introduced by block copolymer micelle nanolithography (BCML) (Figure 1.4e).[55] Self-assembly of gold ion-containing diblock copolymer micelles into hexagonal arrays and a subsequent air plasma treatment produced gold nanoparticles with a diameter of around 5-7 nm on the substrate over which a SLB is formed by vesicle fusion method. This system can control spacing between particles in arrays through changing the polymer molecular weight and does not require complex pattering methods. Gold nanoparticles embedded in SLBs were coupled with various biological molecules via thiol linker molecules. This method allows for protein or other ligands fictionalization on the fluid lipid component (mobile), the fixed nanoparticle (immobile), or both over a large area.

1.2.3 Nanomaterial-tethering Techniques

Nanomaterial tethering to lipid bilayers involves a connection between a nanomaterial and the head of the bilayer. The first nanomaterial bilayer

linking paper by G. M. Lee et al. introduced adsorbing an antibody against fluorescein onto the surface of a 30 nm gold nanoparticle, and allowing it to attach to a bilayer consisting of 1.7 mol% fluorescein-labeled lipids while maintaining the mobility.[56] Mascalchi et al. used streptavidin or NeutrAvidin-coated particles, such as latex, quantum dots, or gold cores, but in lieu of linking them by biotin–streptavidin (NeutrAvidin), they used a biotinylated antibody against fluorescein (Figure 1.5a).[57] This enabled a tether to a fluorescein containing bilayer, similar to the original tethering technique pioneered by G. M. Lee et al .[56]

Positive proteins besides antibodies also adsorb well onto the negatively charged surface of citrate-capped gold nanoparticles, and nanoparticles adsorbed proteins or antibodies form linkages to the bilayer surface by protein-protein or antigen- antibody interaction. For example, the tetrameric streptavidin can be adsorbed onto gold nanoparticles and linked to a bilayer containing a low percentage (≤1 mol%) of lipids modified by biotin on heads.[58] The binding interaction between biotin and streptavidin (or its variants avidin and NeutrAvidin) forms strong noncovalent bond and has been used successfully to create fluidic nanomaterials on bilayers by stably-linked protein.[59-61] Y. K. Lee et al. densely packed gold nanoparticles with thiolated DNA oligomers and some of which were capped with biotin to enable and control linking process to a biotin–streptavidin bilayer (Figure 1.5b).[62] Besides gold nanomaterials, the thiol group is reactive to other species available for linking methods. For example, Murcia et al. modified CdSe/ZnS core–shell quantum dots with hydrophilic groups and maleimide, the latter of

which reacts with thiolated lipids to make a covalent bond.[63]

Hsieh et al. and Spillane et al. used streptavidin-adsorbed gold nanoparticles reacted the particles with biotinylated cholera toxin subunit B (CTB) in solution.[64] The particles were next incubated to a bilayer containing ganglioside lipid (GM1), which linked the natural ligand of CTB to the receptor of GM1 by the receptor–ligand interaction (Figure 1.5c).

A subsequent paper by Yoshina-Ishii et al. provided a gentler linking technique induced by DNA hybridization. Oligonucleotides were conjugated to lipid headgroups, and these modified lipids were able to spontaneously inset into preformed SLBs and lipid vesicles.[65] The modified lipid insertion also created a mobile display of tethered lipid vesicles using DNA hybridization (Figure 1.5d). Benkoski and Höök took a similar approach but instead used cholesterol-tagged DNA.[66] Following the spontaneous insertion of the cholesterol into preformed vesicles and SLBs, DNA hybridization also produced the mobility of tethered vesicles. For vesicles with a more robust DNA tether, van Lengerich et al. (2010) devised a DNA templated click reaction to attach the vesicles' DNA covalently to the SLB.[67] Compared to the previous tethering techniques which relied on DNA hybridization alone, this orthogonal covalent linkage has the advantage of stability under different buffer conditions, as low salt concentrations destabilize DNA base pairing.

The above studies represent a range of bilayer linking techniques for nanomaterials that can be easily applied or combined into new strategies. It is important not only the tether's composition but also physical behavior such as mobility control function for controlling the number of tethers per particle.

This number exists on a continuum where a nanomaterial with several attachment points to a bilayer will exhibit limited or no mobility, even on a fluid bilayer. At the other extreme, a nanomaterial with very few, or just one attachment, will diffuse freely on a fluid bilayer. Thus, a successful bilayer platform of tethered nanomaterials involves controlling this degree of attachment. Part of this requires an optimal concentration of linking lipids, which are mixed into the bilayer constituent lipids at concentrations ranging from 0.1 to 4 mol% depending on the chemistry involved.[68, 69] For some experiments, it is more important to regulate the surface chemistry to reduce the number of surface anchoring sites. This was key for the original tethering by G. M. Lee et al. where mobile attachment was not achieved until blocking most of the fluorescein antibodies on the nanoparticle with a secondary antibody.[56] Also limiting multiple tether formation, Y. K. Lee et al. used 1 : 799 molar ratio of biotinylated DNA to target captured DNA on their nanoparticles to produce a highly mobile attachment with an assumed single anchor on a bilayer with 0.1 mol% biotin–streptavidin while 200 : 600 molar ratio to occur immobile attachment.[62]

1.3. Nanomaterial-tethered SLB-Based Bioapplications

Recently, nanomaterials were tethered to lipid bilayers by convenient and simple linking system. This concept provided a nanomaterial-tethered 2D supported lipid bilayer technique for easily studying dynamics of biomolecules interaction. The target-binding-induced changes of nanomaterials on 2D fluidic membrane were conveniently observed by fluorescence or dark-field microscopy (DFM). Observed kinetic informations allowed biomolecules to detect and quantify or analyze in bio-environment.

In biosensors, a single Au nanoparticles (NPs) tracking-based method on an SLB platform allowed for detecting and quantifying molecular binding to membrane receptor-binding targets of interest.[68] When ligand molecules (CTB in this case) are bound to ganglioside GM1 on SLB, the gel-phase lipid domains are formed, and AuNP mobility was subsequently affected by bulky, multivalent CTB binding to ganglioside GM1 on SLB (Figure 1.6a). The target-binding-induced change in the membrane fluidity was evaluated using DFM-based single nanoparticle tracking of AuNPs linked to supported lipid bilayer to detect the concentration of CTB in solution. Importantly, when paucivalent AuNPs that have much less thiolated lipid-binding area are used as detection labels, higher diffusion coefficient values, better sensitivity, and wider dynamic range were obtained than when multivalent AuNPs were used as detection labels. The detection limit using this paucivalent NPs for CTB targets was almost 10 pM without optimization. Moreover, the dynamic range for this method is from 10 pM to 100 nM.

By using biotin-streptavidin interaction, a large number of AuNPs can be

reliably and stably tethered to a SLB. AuNPs stably modified by the reasonable molar ratio of thiolated target capture oligonucleotides and thiolated SLB tethering oligonucleotides allows for massively parallel *in situ* analysis of the hybridization of target sequence between the nanoprobes with single-particle resolution on a two-dimensional (2D) fluidic surface (Figure 1.6b).[62] As an application example, they performed a DNA detection assay with promising sensitivity and dynamic range (high attomolar to high femtomolar) without optimization, as well as remarkable single-base mismatch discrimination capability. In another instance of biotin-streptavidin linking system, metal NPs with three distinct dark-field light scattering signals [red (R), green (G), and blue (B)] and three different target miRNA half-complements were tethered to a two dimensionally fluidic SLB with mobile (M) or immobile (I) state (Figure 1.6c).[70] *In situ* single-particle monitoring and normalized RGB analysis of the optokinetically combinatorial assemblies among three M-NPs and three I-NPs with DFM allow for differentiating and quantifying 9 different miRNA targets in one sample. The OK-NP-based assay enables simultaneous detection of multiple miRNA targets in a highly quantitative, specific manner within 1 h and can be potentially used for diagnosis of different cancer types.

Membrane–membrane recognition and binding are significant in various biological processes. They suggest a method to understanding the dynamics of such reactions by using DNA-tethered vesicles as a general scaffold for displaying membrane components.[71] This platform was used to analyze the docking reaction between two populations of tethered vesicles that display

complementary DNA. Deposition of vesicles onto a SLB was performed by using a microfluidic device to obstruct mixing of the vesicles in bulk during sample preparation. Once tethered onto the surface, vesicles mixed via two-dimensional diffusion. DNA-mediated docking of two reacting vesicles results in their colocalization after collision and their subsequent tandem motion. Individual docking events and population kinetics were observed via epifluorescence microscopy. A lattice-diffusion simulation was implemented to extract from experimental data the probability, P_{dock}, that a collision leads to docking. For individual vesicles displaying small numbers of docking DNA, P_{dock} shows a first-order relationship with copy number as well as a strong dependence on the DNA sequence. Both trends are explained by a model that includes both tethered vesicle diffusion on the supported bilayer and docking DNA diffusion over each vesicle's surface. These results provide the basis for the application of tethered vesicles to study other membrane reactions including protein-mediated docking and fusion.

1.4. Conclusion and perspective

We briefly report various nanomaterial-tethered SLB studies that consist of formation methods of 2D SLB, bilayer-tethered nanomaterial techniques, and a wide spectrum of bioapplication. Use of the fluidity on 2D supported lipid bilayer will continue to play an important role in the development of sensors and nanodevices for kinetic analysis between biomolecules. If developed to a stable and commercial level, biosensors using SLB have the potential to accelerate research in the field of proteomics and genomics sensors. Previous biotechnology has been difficult to analyze sensitively dynamic reactions between biomolecules such as DNA or RNA reaction, hybridization and dissociation, and protein interaction, antigen-antibody or protein-small molecule interaction. However, nanomaterial-tethered SLB techniques take advantage of the fluidity on artificial cell membrane, which reproduces subtle dynamic reactions of biomolecules. Through simple and convenient observation methods, they can offer opportunities for the study and analysis of many biologically important issues, such as kinetics between biopolymers. With expanding research in nanomaterials, SLB, and detection techniques, we believe that the combination of nanomaterials with SLB will continue to produce unique results relating to dynamics, biophysics, and biosensing application.

1.5. References

1. Chan, Y.-H.M. & Boxer, S.G. *Curr. Opin. Chem. Biol.* **11**, 581-587 (2007).
2. Castellana, E.T. & Cremer, P.S. *Surf. Sci. Rep.* **61**, 429-444 (2006).
3. Tanaka, M. & Sackmann, E. *Nature* **437**, 656-663 (2005).
4. Lee, Y.K. & Nam, J.M. *Small* **8**, 832-837 (2012).
5. Nam, J.M., Nair, P.M., Neve, R.M., Gray, J.W. & Groves, J.T. *Chembiochem* **7**, 436-440 (2006).
6. Liu, C.M., Monson, C.F., Yang, T.L., Pace, H. & Cremer, P.S. *Anal. Chem.* **83**, 7876-7880 (2011).
7. Lee, Y.K., Lee, H. & Nam, J.-M. *NPG Asia Mater.* **5**, e48 (2013).
8. Tamm, L.K. & McConnell, H.M. *Biophys. J.* **47**, 105-113 (1985).
9. Johnson, S.J., Bayerl, T.M., McDermott, D.C., Adam, G.W., Rennie, A.R., Thomas, R.K. & Sackmann, E. *Biophys. J.* **59**, 289-294 (1991).
10. Lagerholm, B.C., Starr, T.E., Volovyk, Z.N. & Thompson, N.L. *Biochemistry* **39**, 2042-2051 (2000).
11. Cremer, P.S. & Boxer, S.G. *J. Phys. Chem. B* **103**, 2554-2559 (1999).
12. Zasadzinski, J., Helm, C., Longo, M., Weisenhorn, A., Gould, S. & Hansma, P. *Biophys. J.* **59**, 755-760 (1991).
13. Egawa, H. & Furusawa, K. *Langmuir* **15**, 1660-1666 (1999).
14. Starr, T.E. & Thompson, N.L. *Langmuir* **16**, 10301-10308 (2000).
15. Ajo-Franklin, C.M., Kam, L. & Boxer, S.G. *P. Natl. Acad. Sci. U.S.A.* **98**, 13643-13648 (2001).
16. Rossetti, F.F., Bally, M., Michel, R., Textor, M. & Reviakine, I.

Langmuir **21**, 6443-6450 (2005).

17. Reimhult, E., Höök, F. & Kasemo, B. *Langmuir* **19**, 1681-1691 (2003).

18. Stelzle, M., Weissmüller, G. & Sackmann, E. *J. Phys. Chem.* **97**, 2974-2981 (1993).

19. Csúcs, G. & Ramsden, J.J. *BBA. Biomembranes* **1369**, 61-70 (1998).

20. Yang, J. & Kleijn, J.M. *Biophys. J.* **76**, 323-332 (1999).

21. Gritsch, S., Nollert, P., Jähnig, F. & Sackmann, E. *Langmuir* **14**, 3118-3125 (1998).

22. Bunjes, N., Schmidt, E., Jonczyk, A., Rippmann, F., Beyer, D., Ringsdorf, H., Gräber, P., Knoll, W. & Naumann, R. *Langmuir* **13**, 6188-6194 (1997).

23. Lahiri, J., Kalal, P., Frutos, A.G., Jonas, S.J. & Schaeffler, R. *Langmuir* **16**, 7805-7810 (2000).

24. Salamon, Z., Wang, Y., Tollin, G. & Macleod, H.A. *BBA. Biomembranes* **1195**, 267-275 (1994).

25. Puu, G. & Gustafson, I. *BBA. Biomembranes* **1327**, 149-161 (1997).

26. Brian, A.A. & McConnell, H.M. *P. Natl. Acad. Sci. U.S.A.* **81**, 6159-6163 (1984).

27. McConnell, H.M., Watts, T.H., Weis, R. & Brian, A.A. *BBA. Reviews on Biomembranes* **864**, 95-106 (1986).

28. Kalb, E., Frey, S. & Tamm, L.K. *BBA. Biomembranes* **1103**, 307-316 (1992).

29. Langmuir, I. *Transactions of the Faraday Society* **15**, 62-74 (1920).

30. Petty, M.C. (Cambridge University Press, 1996).

31. Hope, M., Bally, M., Webb, G. & Cullis, P. *BBA. Biomembranes* **812**, 55-65 (1985).

32. Mayer, L., Hope, M. & Cullis, P. *BBA. Biomembranes* **858**, 161-168 (1986).

33. Nayar, R., Hope, M.J. & Cullis, P.R. *BBA. Biomembranes* **986**, 200-206 (1989).

34. Frisken, B., Asman, C. & Patty, P. *Langmuir* **16**, 928-933 (2000).

35. Barenholz, Y., Gibbes, D., Litman, B., Goll, J., Thompson, T. & Carlson, F. *Biochemistry* **16**, 2806-2810 (1977).

36. Mimms, L., Zampighi, G., Nozaki, Y., Tanford, C. & Reynolds, J. *Biochemistry* **20**, 833-840 (1981).

37. Roessner, C.A., Struck, D.K. & Ihler, G.M. *J. Biol. Chem.* **258**, 643-648 (1983).

38. Johnson, J.M., Ha, T., Chu, S. & Boxer, S.G. *Biophys. J.* **83**, 3371-3379 (2002).

39. Hamai, C., Yang, T., Kataoka, S., Cremer, P.S. & Musser, S.M. *Biophys. J.* **90**, 1241-1248 (2006).

40. Berquand, A., Mazeran, P.-E., Pantigny, J., Proux-Delrouyre, V., Laval, J.-M. & Bourdillon, C. *Langmuir* **19**, 1700-1707 (2003).

41. Crane, J.M., Kiessling, V. & Tamm, L.K. *Langmuir* **21**, 1377-1388 (2005).

42. Stelzle, M., Miehlich, R. & Sackmann, E. *Biophys. J.* **63**, 1346-1354 (1992).

43. Cha, T., Guo, A. & Zhu, X.-Y. *Biophys. J.* **90**, 1270-1274 (2006).

44. Groves, J.T., Ulman, N. & Boxer, S.G. *Science* **275**, 651-653 (1997).

45. Kam, L. & Boxer, S.G. *J. Am. Chem. Soc.* **122**, 12901-12902 (2000).

46. Kung, L.A., Groves, J.T., Ulman, N. & Boxer, S.G. *Adv. Mater.*. **12**, 731-734 (2000).

47. Groves, J.T. & Boxer, S.G. *Acc. Chem. Res.* **35**, 149-157 (2002).

48. Nair, P.M., Salaita, K., Petit, R.S. & Groves, J.T. *Nat. Protoc.* **6**, 523-539 (2011).

49. Salaita, K., Wang, Y.H. & Mirkin, C.A. *Nat. Nanotechnol.* **2**, 145-155 (2007).

50. Salaita, K., Wang, Y.H., Fragala, J., Vega, R.A., Liu, C. & Mirkin, C.A. *Angew. Chem. Int. Edit.* **45**, 7220-7223 (2006).

51. Narui, Y. & Salaita, K.S. *Chem. Sci.* **3**, 794-799 (2012).

52. Lenhert, S., Sun, P., Wang, Y.H., Fuchs, H. & Mirkin, C.A. *Small* **3**, 71-75 (2007).

53. Sekula, S., Fuchs, J., Weg-Remers, S., Nagel, P., Schuppler, S., Fragala, J., Theilacker, N., Franueb, M., Wingren, C., Ellmark, P., Borrebaeck, C.A.K., Mirkin, C.A., Fuchs, H. & Lenhert, S. *Small* **4**, 1785-1793 (2008).

54. Shi, J.J., Chen, J.X. & Cremer, P.S. *J. Am. Chem. Soc.* **130**, 2718-+ (2008).

55. Lohmuller, T., Triffo, S., O'Donoghue, G.P., Xu, Q., Coyle, M.P. & Groves, J.T. *Nano. Lett* .**11**, 4912-4918 (2011).

56. Lee, G.M., Ishihara, A. & Jacobson, K.A. *P. Natl. Acad. Sci. U.S.A.*

88, 6274-6278 (1991).

57. Mascalchi, P., Haanappel, E., Carayon, K., Mazères, S. & Salomé, L. *Soft Matter* **8**, 4462-4470 (2012).

58. Lin, Y.-H., Chang, W.-L. & Hsieh, C.-L. *Opt. Express* **22**, 9159-9170 (2014).

59. Salaita, K., Nair, P.M., Petit, R.S., Neve, R.M., Das, D., Gray, J.W. & Groves, J.T. *Science* **327**, 1380-1385 (2010).

60. Laitinen, O., Hytönen, V., Nordlund, H. & Kulomaa, M. *Cell. Mol. Life Sci.* **63**, 2992-3017 (2006).

61. Nam, J.M., Nair, P.M., Neve, R.M., Gray, J.W. & Groves, J.T. *ChemBioChem* **7**, 436-440 (2006).

62. Lee, Y.K., Kim, S., Oh, J.W. & Nam, J.M. *J. Am. Chem. Soc.* **136**, 4081-4088 (2014).

63. Murcia, M.J., Minner, D.E., Mustata, G.-M., Ritchie, K. & Naumann, C.A. *J. Am. Chem. Soc.* **130**, 15054 (2008).

64. Spillane, K.M., Ortega-Arroyo, J., de Wit, G., Eggeling, C., Ewers, H., Wallace, M.I. & Kukura, P. *Nano Lett.* **14**, 5390 (2014).

65. Yoshina-Ishii, C., Miller, G.P., Kraft, M.L., Kool, E.T. & Boxer, S.G. *J. Am. Chem. Soc.* **127**, 1356-1357 (2005).

66. Benkoski, J.J. & Höök, F. *J. Phys. Chem. B* **109**, 9773-9779 (2005).

67. van Lengerich, B., Rawle, R.J. & Boxer, S.G. *Langmuir: the ACS journal of surfaces and colloids* **26**, 8666 (2010).

68. Yang, Y.-H. & Nam, J.-M. *Anal. Chem.* **81**, 2564-2568 (2009).

69. Sagle, L.B., Ruvuna, L.K., Bingham, J.M., Liu, C., Cremer, P.S. &

Van Duyne, R.P. *J. Am. Chem. Soc.* **134**, 15832 (2012).

70. Kim, S., Park, J.-E., Hwang, W., Seo, J., Lee, Y.-K., Hwang, J.-H. & Nam, J.-M. *J. Am. Chem. Soc.* **139**, 3558-3566 (2017).

71. Chan, Y.-H.M., Lenz, P. & Boxer, S.G. *P. Natl. Acad. Sci. U.S.A.* **104**, 18913-18918 (2007).

72. Shi, J., Chen, J. & Cremer, P.S. *J. Am. Chem. Soc.* **130**, 2718-2719 (2008).

73. Lohmüller, T., Triffo, S., O'Donoghue, G.P., Xu, Q., Coyle, M.P. & Groves, J.T. *Nano Lett.* **11**, 4912-4918 (2011).

74. Hartman, K.L., Kim, S., Kim, K. & Nam, J.-M. *Nanoscale* **7**, 66-76 (2015).

75. Hormel, T.T., Kurihara, S.Q., Brennan, M.K., Wozniak, M.C. & Parthasarathy, R. *Phys. Rev. Lett.* **112**, 188101 (2014).

76. Hsieh, C.-L., Spindler, S., Ehrig, J. & Sandoghdar, V. *J. Phys. Chem. B* **118**, 1545-1554 (2014).

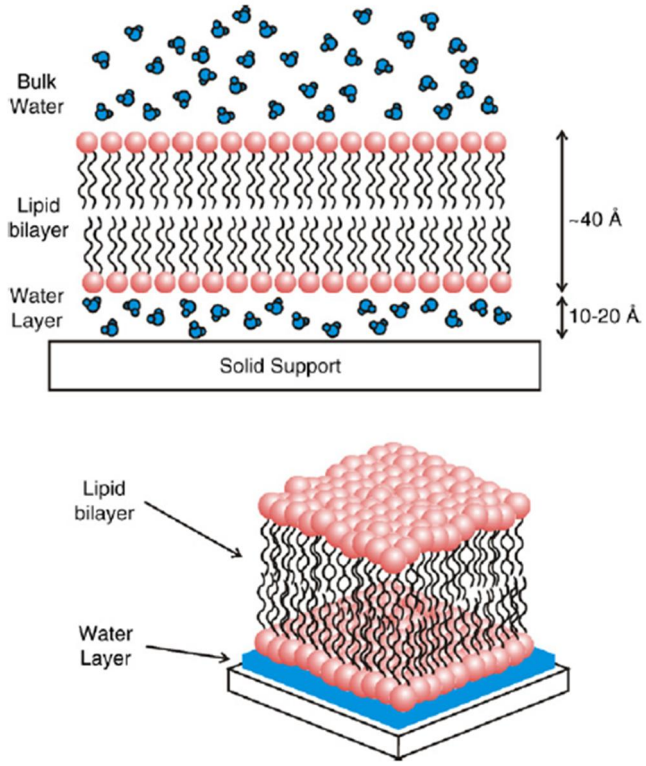

Figure1.1. Schematic diagram of a solid supported lipid bilayer. The membrane is separated from the substrate by a 10–20 Å thick layer of water.[8]

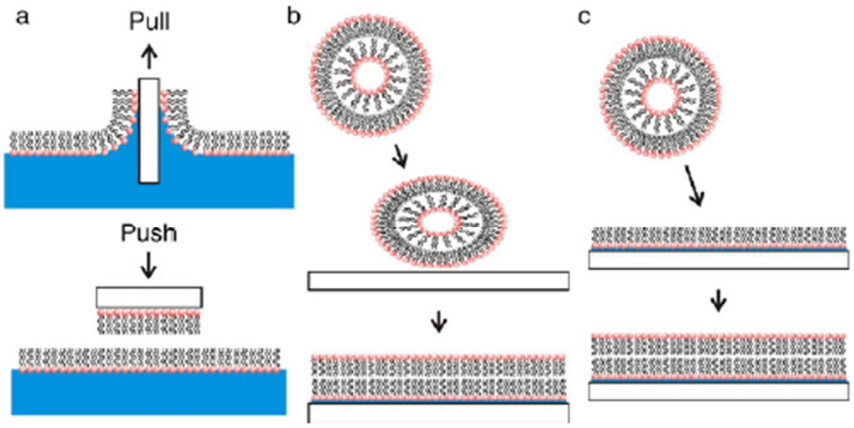

Figure 1.2. Common techniques for the formation of supported lipid bilayers. (a) The Langmuir–Blodgett technique is carried out by pulling a hydrophilic substrate through a lipid monolayer and sequentially pushing it horizontally through another lipid monolayer. (b) Vesicles in solution adsorb and spontaneously fuse to the surface to form a solid supported lipid bilayer. (c) A combination of the Langmuir–Blodgett and vesicle fusion processes.[2]

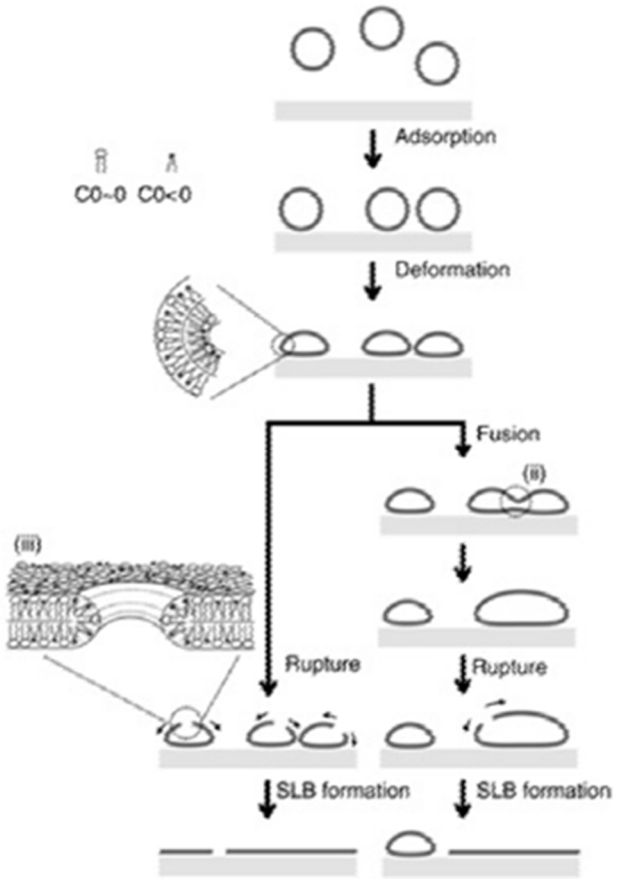

Figure 1.3. Proposed method of vesicle fusion. Adsorbed vesicles deform and either rupture or fuse with one another to form larger vesicles which in turn rupture to form a continuous surface supported membrane.[39]

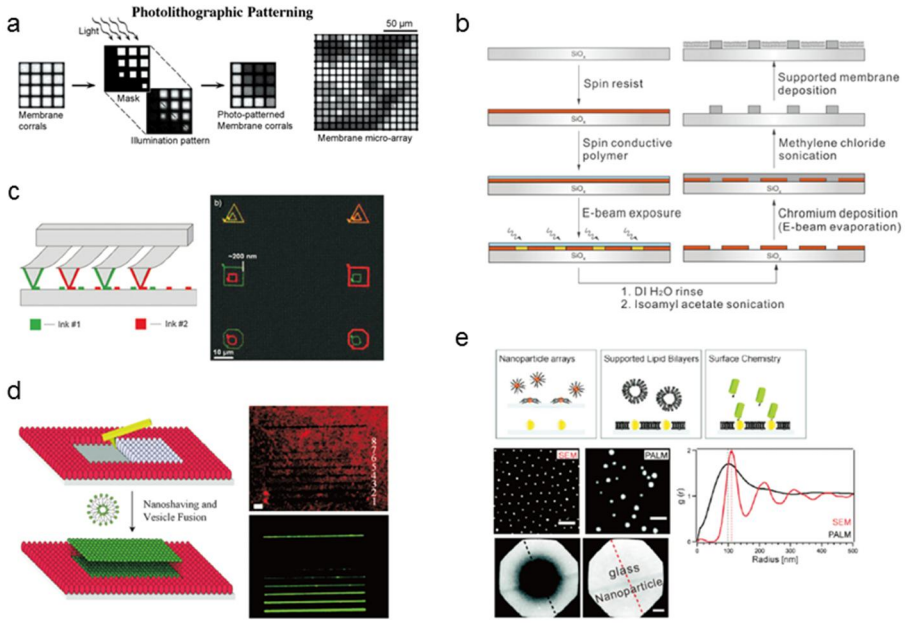

Figure 1.4. Micropatterning fluid lipid bilayers on solid supports (a) Composition arrays generated by photopatterning.[47] A mask is used to selectively bleach different sized areas of a membrane array. After diffusive mixing within each corral, a concentration array is observed. (b) Fabrication of metal lines using electron beam lithography and the subsequent formation of patterned lipid bilayers.[48] (c) Left: schematic illustration of parallel patterning of different lipids on subcellular scales with a multiplexing dip-pen nanolithography (DPN) cantilever array. Right: fluorescence images of multilayered 1,2-dioleoyl-sn glycero-3-phosphocholine (DOPC) structures containing fluorophore-labeled lipids (rhodamine/red and fluorescein/green).[53] (d) Left: schematic illustration of atomic force microscopy (AFM)-based nanoshaving lithography for nanoscale supported lipid bilayer (SLB) formation. Right: epifluorescence images of a nanoshaved bovine serum

albumin (BSA) monolayer (top) and SLB lines (bottom). The scale bar is 3 mm.[72] (e) Top: schematic overview of nanoparticle array-embedded SLBs. Middle: from the left, reference SEM image of gold nanoparticle arrays and photoactivated localization microscopy (PALM) image of individual ephrin-mEos-His10 molecules conjugated on the same gold nanoparticle array. The scale bar is 200nm in both cases. The right figure represents comparison of the radial distribution function from the full PALM image (black) and the reference SEM image (red). Bottom: fluorescence recovery after photobleaching (FRAP) on a bilayer of DOPC doped with 0.5% Texas Red-1,2-dihexadecanoyl-sn-glycero-3 phosphoethanolamine (DHPE).[73]

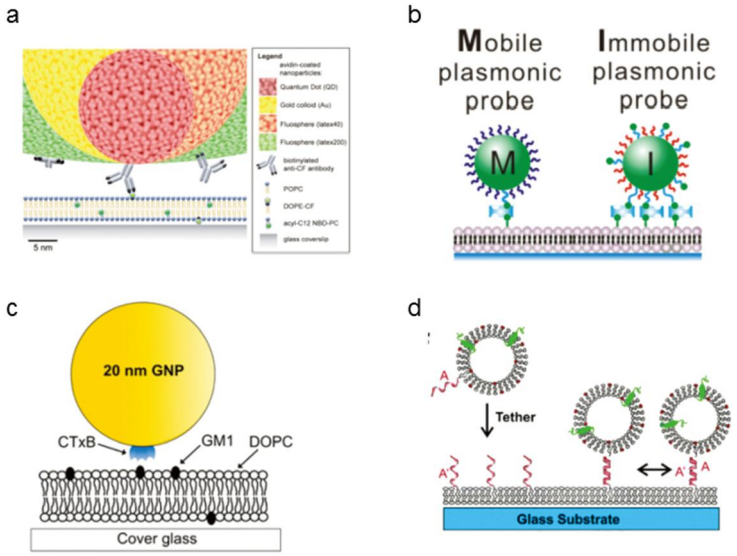

Figure 1.5. Various techniques to tether nanomaterials onto SLBs.[74] (a) Scale illustration of different antibody-adsorbed particles for attachment to fluorescent lipids in a SLB.[57] (b) Biotin DNA-modified gold nanoparticles binding to biotinylated-SLB with streptavidin.[75] (c) CTB (i.e. CTxB)-modified gold nanoparticle with GM1-lipid. The gold nanoparticle is functionalized with streptavidin, and then reacted with a concentration of biotinylated CTB to achieve an average of one CTB pentamer per particle.[76] (d) DNA-modified vesicle hybridizing and tethering to a DNA-modified SLB.[65]

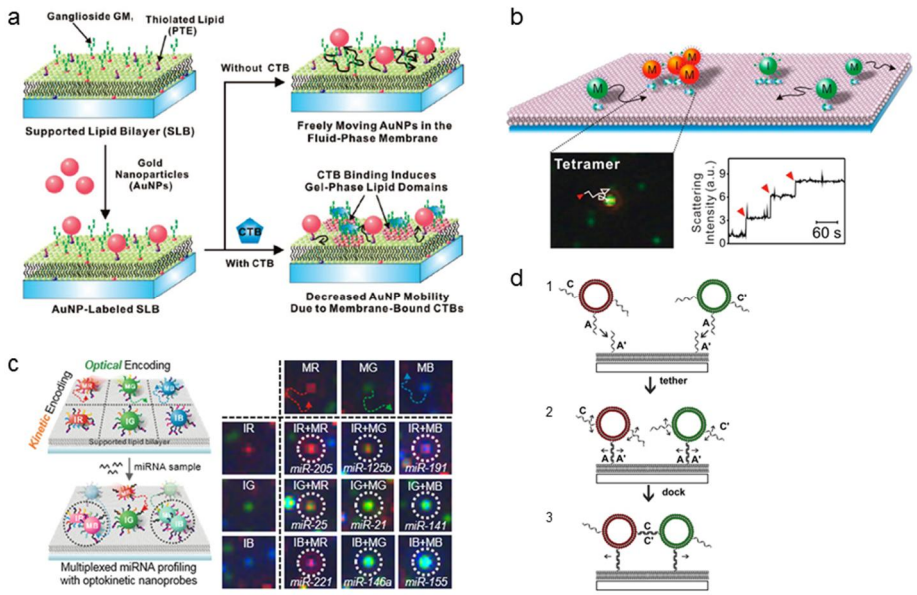

Figure 1.6. (a) Single nanoparticle tracking-based detection on supported lipid bilayer platform and time-lapse dark-field images of lipid-tethered AuNPs on supported lipid bilayer.[68] (b) Schematic illustration of dynamic two dimensional confinement of plasmonic nanoparticles on lipid bilayer surface. Two different types of probes (mobile and immobile plasmonic probes) are tethered to a supported lipid bilayer. Target DNA hybridization induces two dimensional cluster formation and plasmonic coupling. Dark-field microscopic images of target DNA hybridization-induced plasmonic nanoparticle clusters. Representative time traces of the scattering intensity for assembly processes of nanoparticle clusters.[62] (c) Optokinetically encoded nanoprobe (OK-NP)-tethered supported lipid bilayer (SLB) assay (OK-NLB assay). The miRNA sample is directly injected into a reaction chamber, and NP interactions are monitored with dark-field microscopy (DFM). Six types of OK-NPs are prepared by kinetic [mobile (M) and immobile (I)] and optical

[red (R), green (G), and blue (B)] coding methods. OK-NPs are composed of plasmonic nanoparticle core, multiple target capture DNAs, and biotinylated DNA. The NP assembly events between the M-NPs and the I-NPs are mediated by target miRNAs and identified with scattering color changes via plasmonic coupling. The nineplexing strategy using combinatorial assemblies between OK-NPs relies on each assembly mode, which was mediated by 9 different target miRNAs.[70] (d) Graphical illustration of vesicles being tethered to a supported bilayer and subsequent DNA-mediated docking between tethered vesicles. (*1*) Vesicles with a tethering DNA (sequence A) and docking DNA (sequence C or C′) are incubated with a supported bilayer that displays the complementary tethering DNA (sequence A′). (*2*) Hybridization of A and A′ tethers the vesicles to the supporting bilayer, and the vesicles are free to diffuse in the plane of the supported bilayer. Tethered vesicle diffusion and diffusion of the docking DNA on the vesicles' surfaces are illustrated with arrows. (*3*) Collisions between vesicles can lead to docking of tethered vesicles via hybridization of C and C′ DNA.[71]

Chapter 2

Dynamic Analysis on Whole Nanoparticle Cumulative Binding Events for Highly Reliable Detection and Quantification of Trace Amounts of DNA

2.1. Introduction

Development of biotechnological methods for quantification of extremely low-abundance biomolecules is increasingly needed for applications such as early, accurate diagnosis or adjuvant therapy for cancers, residual micrometastatic disease or minimal residual disease (MRD)[1, 2], detection of minimal amounts of quantifiable DNA during forensic investigations, and ultrasensitive screening of biowarfare agents[3], but several key challenges still remain. Although a number of ultrasensitive bioassays have been developed recently[3-10], enzymatic DNA amplification-based PCR has been the dominantly used method for reliable detection of extremely low concentrations of target molecules, especially for clinical applications. PCR has an ultra-low limit of detection in the range of tens to thousands of molecules, but also has the potential to generate false positive signals from even a subtle contamination, needs a proper primer pair for each case[11], and requires tedious experimental steps with temperature control.

For amplification-free and more accurate detection of ultra-low-abundance target molecules, the signals that transduce binding events should be strong and reproducible for reliable analysis. In addition, the sensing strategy should shift from the conventional ensemble-averaged measurement in bulk samples to the single-molecule/single-particle-level counting of binding events between target molecules and recognition sites. Biological binding reactions involving a ultra-small quantity are stochastic in nature, out of equilibrium, and resulting in fluctuations with a low signal-to-noise (S/N)

ratio[12]. Moreover, the binding processes and analysis are hindered by diffusion limitations, random 3D motions in solution, slow binding, and the frequent dissociation of complexed molecules[12-14]. Accordingly, efficient signal enhancement and detection with high S/N ratio for analyzing target binding events and a clear differentiation of target recognition-induced signal change from non-specific binding-induced signal change while minimizing specific target binding-based signal loss are needed to allow the quantification of low-abundance biomolecules with high confidence. It should be also noted that heavily used fluorescent labels[15-18] are prone to photobleaching and photoblinking, which prevent long-term monitoring, accurate signal acquisition, and highly reliable quantification of small amounts of molecules[19, 20], and signal amplifying nanoprobes such as metal-enhanced fluorescence and surface-enhanced Raman scattering probes require complex structural design, highly precise synthesis of targeted structures in a high yield, and complicated bioconjugation strategies[21, 22].

Here, we present a dynamic biomolecule binding analysis method that allows for maximally detecting target binding signals while clearly differentiating target-specific binding from non-specific binding, called dynamic analysis on whole nanoparticle cumulative binding events (DANCE; Figure 2.1). DANCE is based on dark-field scattering signal detection from single-nanoparticles (NPs) on 2D supported lipid bilayer (SLB), analyzes dynamically binding and dissociating NPs on lipid bilayer micropattern (NLM) in real time, and circumvents many of the above-mentioned issues.

Importantly, DANCE minimizes detection signal loss by incorporating weak target binding and dissociation processes in a time-dependent manner and analyzing whole NPs on a micropattern with dark-field microscopy, which are critical for obtaining detection signals from an ultra-low abundance of biomolecules without a need for enzymatic amplification or signal amplification process. A key concept is defining target binding-induced NP dimer species that include bound dimers and dissociating dimers differentiating them from transient and nonspecific binding species (Figure 2.1c). The results show that DANCE allows for reliably detecting and quantifying 10s-1000s of anthrax DNA in samples without a need for any enzymatic or signal amplification process.

2.2. Experimental Section

Material: 1,2-dioleoyl-sn-glycero-3-phosphochline (DOPC), 1,2-dioleoyl-sn-glycero-3-phosphoethanolamine-N-[methoxy(polyethylene glycol)-1000] ammonium salt (PEG-DOPE) were obtained from Avanti Polar Lipids (Alabaster, AL, USA). Streptavidin (STV) was obtained from Molecular Probes (Eugene, OR, USA). Methoxypolyethylene glycol thiol (molecular weight: 1000 Da) was purchased from Laysan Bio Inc. (Arab, AL, USA). Bovine serum albumin (BSA), sodium dodecyl sulfate (SDS) and dithiothreitol (DTT) were purchased from Sigma-Aldrich (St. Louis, MO, USA). Phosphate-buffered saline (PBS) solution (0.15 M) was prepared by dissolving NaH_2PO_4, Na_2HPO_4, and NaCl (Sigma-Aldrich, St. Louis, MO, USA) in DI water, yielding 10 mM phosphate-buffered solution with 150 mM NaCl (pH 7.4). 0.025 M PBS was prepared, containing 25 mM NaCl with the same reagents. Nanopure water with the minimum resistance (>18 $M\Omega \cdot cm^{-1}$) was applied to all the experiments. For the lipid vesicle preparation (vesicle extrusion), polycarbonate (PC) filters (Whatman, Fisher Scientific) with a pore diameter of 100 nm were used. Organic solvents such as chloroform, acetone, and ethanol were obtained from Duksan Pure Chemicals Co. Ltd. (Gyeongi-do, South Korea). Gold nanoparticles (50 nm) and oligonucleotides were obtained from BBI Life Sciences (Cardiff, UK) and Integrated DNA Technology (Coralville, IA, USA), respectively. Commercial human serum (from human male AB plasma, USA origin, sterile-filtered) was purchased from Sigma-Aldrich.

Preparation of about small unilamellar vesicles (SUV): In a 50 mL

round–bottomed flask, 97.1 mol% DOPC, 0.4 mol% biotinylated DOPE, and 2.5 mol% PEG-DOPE were mixed in chloroform. This lipid solution was evaporated by a rotary evaporator. Using a stream of N_2, the lipid film was completely dried. The thoroughly dried solution was resuspended in DI water and added into a cryo-tube for subjecting to three repetitive freeze-thaw cycles. The final lipid concentration was 4 $mg \cdot mL^{-1}$. The solution was extruded exactly 21 times through a polycarbonate (PC) membrane with a pore diameter of 100 nm at room temperature. Approximately 100 nm liposome was kept at 4°C until use.

Functionalization of paucivalent mobile and polyvalent immobile Au-nanoprobes with control of ratio between target capture and biotin DNA: Using 100 mM dithiothreitol (DTT) in 100 mM phosphate buffer (PB) solution (pH 8.3), thiolated oligonucleotides were reduced for 2 h and utilizing a NAP-5 column (GE Healthcare, Buckinghamshire, U.K.), they were separated from impurities. For DNA functionalization, immediately reduced oligonucleotides and 50 pM of 50-nm AuNPs were mixed with the rational molar ratio of supported lipid bilayer (SLB) tethering sequence (biotinylated sequence) and target capture sequence and incubated at room temperature overnight. For immobile Au-nanoprobes (i-NPs), the molar ratio was 200:600. For mobile Au-nanoprobes (m-NPs), the molar ratio was 1:799. The final solution was adjusted to produce 0.5 M PBS with 0.01% (w/v) sodium dodecyl sulfate (SDS) by adding 2 M NaCl with 0.01% (w/v) SDS (salting solution) in 0.05 and 0.1 M incremental steps. After each addition of salting solution, the solution was heated at 65°C for 10 min and incubated for

30 min at room temperature. The DNA−AuNP mixture was allowed to keep overnight at room temperature and then the solution was centrifuged (5000 rpm, 10 min). The supernatant was removed and the remainder was redispersed in DI water (this procedure was repeated three times). The DNA-functionalized AuNP solution was kept at 4°C until use.

Fabrication of patterned SLB for whole behavior observation of all Au-nanoprobes: For analysis using NLM system, A 120 × 120 μm^2 patterned chrome film on a cover glass was fabricated by conventional photolithography and followed by lift-off process. Adding SUV solution produced selective deposition of a SLB onto an exposed glass surface because it was difficult to form SLB on chrome film (Figure 2.1).

Preparation of fluidic SLB and modification of Au-nanoprobes to SLB and DNA detection assay: SLB and Au nanoprobes bound to SLB were prepared using a 120 × 120 μm^2 patterned chrome film in small chamber with inner radius of 1 mm on a cover glass. A Cr patterned glass substrate was cleaned by sonication for 10 min each, in AZ700 remover, acetone, chloroform, acetone, and DI water. After washing, the substrate was pretreated with 1 M NaOH for 1 h and then washed with DI water 10 times. Before using the substrate, it was thoroughly dried using a N_2 stream. The prepared SUV was mixed 1:1 with 0.15 M PBS placed on the Cr micropatterned glass attached to a small sticker chamber. Approximately 3.5 μL SUV solution was required to fill the small chamber. After 40 min at room temperature, excess and unfused SUVs were removed by washing with 0.15 M PBS three times. Bovine serum albumin (BSA, 2 μM) in 0.15 M PBS solution was added in the

small chamber for 30 min to minimize non-specific binding of Au-nanoprobes attached to other chrome film, except for SLB observed by commercial dark-field microscope (Axiovert 200M, Carl Zeiss, Göttingen, Germany) with a 40× objective lens (NA 0.6) and AxiCam HRc color camera as well as to remove defects on SLB. Optimization concentration of streptavidin (STV, 60 nM) in 0.15 M PBS solution was interacted with biotinylated SLB for 1 h. Unreacted STV was cleaned with 0.15 M PBS and the small chamber was filled with 0.025 M PBS. Next, 40 pM m-NPs probes were introduced and reacted for 30 min. Unlinked m-NPs on SLB were washed with 0.15 M PBS 4 times. Next, the different number of target DNA ranging from 47 (22.5 aM) to 9500 (4.5 fM) strands with 200 fM noncomplementary DNA was reacted with m-NPs tethered to 2-D fluidic supported lipid bilayer micropattern for 8 h in 0.15 M PBS. All control experiments were carried out with 200 fM noncomplementary DNA. 30 pM i-NPs were introduced and reacted for 5 min. Unreacted i-NPs were perfectly eliminated with 0.15 M PBS 4 times in 5 min and unreacted STV binding sites were quenched by washing with 0.15 M PBS containing 1 μM free biotins for 5 min. This usually generates SLB-tethered i-NPs and m-NPs in the ratio of 1:3. For dynamic reaction between single-nanoprobes by a DNA, we monitored binding and dissociation events with DF microscopy in real time and analyzed them through change of scattering intensity and duration time.

Dynamic single-particle analysis on DNA binding and dissociation events with dark-field (DF) microscopy-based in situ monitoring: Mobility and binding and dissociation between all SLB-linked NPs in 2-D fluidic

supported lipid bilayer micropattern (NLM) were tracked using a commercial DF microscope. All the image analysis processes were dealt with ImageJ software (http://rsb.info.nih.gov/ij/). For tracking and trajectory analysis of individual SLB-tethered NPs, the MOSAIC plugin in the imageJ program was used. The scattering intensity was analyzed by the basic intensity measurement of ImageJ software. The brightness and contrast of microscope images are not adjusted unless it is mentioned in the figure caption. Real-time dark-field movie of Au-nanoprobes tethered SLB with each target DNA copy number on 120× 120 μm^2 Cr patterned glass as follows; starting point: 15 min after addition of i-NPs. To select rational time interval between each data was set at 200 ms, 3 min, or 12 min. Using real-time dark-field analysis, we determined optimized time interval resulting from analysis of dissociation distribution and dissociation reaction. For DANCE, the interval time was 12 min. Observation time was 240 min. We identified the types of dimers through observation of scattering intensity and duration time with obtained dimers (Figure 2.2c).

Detection of target anthrax DNA into crude serum: For the experiment in 1% human serum, 10 μL freshly-thawed commercial human serum (from human male AB plasma, USA origin, sterile-filtered, Sigma-Aldrich) was combined with the 27 and 45 aM target anthrax DNA and 200 fM noncomplementary DNA in 990 μL 0.15 M PBS and incubated for 15 min at room temperature. Next, 3.5 μL sample was reacted with m-NPs tethered to a fluidic SLB for 8 h. Control experiments were carried out with 200 fM noncomplementary DNA in the same human serum. Next, 30 pM i-NPs were

introduced and reacted for 5 min. Unreacted i-NPs were removed by washing 4 times with 0.15 M PBS and unreacted STV binding sites were quenched by washing with 0.15 M PBS containing 1 μM free biotins. The results were observed and analyzed as described above.

2.3. Results and Discussion

In a typical biosensing scheme, the initial signal intensity before detecting targets of interest is compared to the final signal intensity after target detection. In our dynamic cumulative detection scheme, however, target-bound nanostructure intermediates are monitored and included as detection signals in a cumulative manner (Figure 2.2a). We employed the total dynamic binding event counting method that include both strong and weak target binding events as detection signals, to increase the assay sensitivity for targets at ultra-low concentrations (Figure 2.2c). The binding reactions occur from the DNA hybridization of target DNA strands with the two half-complementary sequences modified on two kinds of Au nanoparticles (AuNPs), respectively; one is a mobile nanoprobe (m-NP) and the other is an immobile nanoprobe (i-NP) that is a fixed marker on a fluidic SLB surface for counting the binding events (Figure 2.2b). The mobility of nanoprobes was finely tuned by the biotin valency of nanoprobes (Figure 2.3). When the distance between NPs becomes much smaller than the distance between individual particles and fixed by DNA hybridization, the changes in plasmonic coupling-based scattering intensity and color can be detected and analyzed by dark-field microscopy in real time. In a conventional static model, the total number of binding events, N_b, is measured as the total number of dimeric Au nanoprobes formed by the DNA hybridization at a final (pseudo) steady state (the left scheme of Figure 2.2a)[23]. At very low target concentrations, there is little chance for trimers or tetramers to be formed, and

the dissociation reactions of dimers becomes significant for target DNA at ultra-low concentrations[24]. In contrast, DANCE is based on the cumulative binding events (N_b^c), i.e., the total dynamic binding events including the dissociating dimers with extended binding time and the bound dimers that stay bound during observation. Additionally, the NLM platform allows for an analysis on the whole NPs on the lipid pattern (120 μm × 120 μm), which minimizes binding signal loss. Based on plasmonic coupling-induced signal increase and real-time binding signal monitoring, four binding species can be defined in our approach – transient dimers without plasmonic coupling in the diffraction limit, plasmonically coupled transient dimers, dissociating dimers that are eventually released from each other with an extended period of a bound state, and bound dimers (Figure 2.2c). The signals from bound dimers and dissociating dimers were included as detection signals that can be included in N_b^c in our case.

We first confirmed that m-NPs and i-NPs are confined in the SLB micropattern without noticeable aggregations and nonspecific bindings on the Cr barrier area (Figure 2.4a). The sparse light-colored dots on the Cr barrier are not attributed to AuNPs, but to the Cr substrate. The assembly and disassembly of nanoprobes were detected by DF scattering intensity change and duration time of binding in the NLM for >240 min (Figure 2.4). Transient dimeric signals were frequently shown as the transient peaks as m-NPs were briefly coupled to and detached from i-NPs without DNA hybridization in the diffraction limit range [Figure 2.4b; these cases are marked with an asterisk

(*)][23]. A representative dissociating dimer begins to emerge at 51 min and last for 36 min (panel 1 in Figure 2.4a and b). As the distribution of the lifetimes of dissociating dimers (τ_d) suggests in Figure 2.5a, the lifetimes of the dissociating dimers assembled via target DNA hybridization are mostly >12 min, irrespective of the added amount of target DNA. When comparing the distribution of the duration time of bound dimers to the lifetime of dissociating dimers, the dissociating dimers regime is likely to differ from the bound dimer regime**.** To verify the effect of specific DNA hybridization on the dissociation reaction of dissociating dimers, we compared the dissociation kinetics between target DNA and the single-base-mismatched (SBM) DNA in 0.15 M PBS for 240 min. The dissociation kinetics results of the dissociating dimers with perfectly-matched target sequence and SBM sequence, respectively, followed a pseudo-first-order dissociation; however, the dissociation half-life for the dissociating dimers with SBM DNA was much shorter than that with fully-matched target DNA (i.e., 11.7 min with SBM DNA vs. 43.3 min with target DNA), as shown in Figure 2.5b. The significant difference of dissociation kinetics between target sequence and SBM sequence allows for detecting target DNA with an ultra-high specificity on this DANCE platform. Based on the dissociation kinetics considering the distribution of τ_d and dissociation half-life, we chose 12 min as the optimal time interval for quantification of ultra-low amounts of DNA with high specificity because the lifetimes of ~98 % dissociating dimers are longer than 12 min and the average lifetime for detecting SBM DNA is ~12 min. (Figure 2.5a-c). It is noteworthy that the dissociation rate constants with target DNA

at different concentrations are very similar. Further, ~60 % of total dimers were obtained as dissociating dimers with 950 target DNA strands in samples while only ~18 % of total dimers were observed as dissociating dimers in the case of a control experiment containing 200 fM of non-complementary sequence, as shown in Figure 2.5c. Incompletely hybridized dimer intermediates are the main reason for this[25], and the results confirm that a dynamic analysis on dissociating dimers is necessary to sensitively detecting and reliably quantifying DNA at ultra-low concentrations.

Next, the assay results with the static analysis method were compared to the DANCE results on the NLM platform. The static analysis that only included initial and final stages of the assay without dissociating dimers could not differentiate 47 target DNA strands from 95 target DNA strands (Figure 2.6a). In stark contrast, the DANCE approach clearly differentiate the result with 47 target DNA strands from 95 target DNA strands after 153 min incubation (Figure 2.6b and Figure 2.7). When samples with varying DNA concentrations were tested, DANCE method generated a linear relationship with the number of total counted dimers while the static analysis method could not differentiate varying sample concentrations (Figure 2.6c**)**. The normal distribution curves more clearly show the DANCE can allow for obtaining more quantitative results in a much clearer manner for ultra-low DNA concentrations (Figure 2.6d and e). Target quantification capability of DANCE improved considerably with increased incubation time, whereas the quantification capability of the static analysis method did not improve with increased incubation time (Figure 2.8).

DNA concentration-dependent SBM DNA differentiation capability was tested with the DANCE method. In the case of target DNA detection, N_b^c also increased as DNA concentration increased. The N_b^c, however, showed no trend when SBM DNA was used (Figure 2.9a). The results further suggest that the use of DANCE system is key to detecting and quantifying DNA in a highly selective manner. Finally, we tested DANCE with more clinically relevant samples (non-complementary DNA strands (200 fM), 47 target DNA strands or 95 target DNA strands were spiked in 1 % human serum). DANCE clearly offers both sensitivity and selectivity. In DANCE system, control samples were fully discernible from 47 and 95 target DNA cases. The N_b^c values were different for 47 and 95 DNA strands even in human serum environments while it was very difficult to distinguish among control, 47 and 95 DNA cases using the N_b values (Figure 2.9b). Therefore, the discrimination between 47 and 95 strands was demonstrated and it was possible to quantify short target nucleic acid by DANCE in human serum (Figure 2.10 and 11).

2.4. Conclusion

In summary, we developed the DANCE method that is based on the newly introduced transient, dissociating and bound dimer concepts and allows for dynamic and continuous analysis on the whole NP interactions on the NLM. With DANCE, we achieved highly confident, straightforward DNA quantification in the range of tens to thousands of target DNA molecules with high reliability. The DANCE-based binding kinetics information facilitated the discrimination of single-base mismatch in DNA sequence at extremely low concentrations. Finally, tens of target DNA strands in total samples were reliably quantified in human serum. In summary, the DANCE using NLM system provides highly sensitive, reliable quantification, with high selectivity for nucleic acid. This promising platform may help early diagnosis in clinical practice, investigation of kinetics or functionality of biomolecules at the single-molecule level, furthermore, assembly of plasmonic nanoparticles with biomolecules.

2.5. References

1. Marx, V. *Nat. Methods* **11**, 241-245 (2014).
2. Garcia-Murillas, I., Schiavon, G., Weigelt, B., Ng, C., Hrebien, S., Cutts, R.J., Cheang, M., Osin, P., Nerurkar, A. & Kozarewa, I. *Sci. Transl. Med.* **7**, 302ra133 (2015).
3. Nam, J.-M., Stoeva, S.I. & Mirkin, C.A. *J. Am. Chem. Soc.* **126**, 5932-5933 (2004).
4. Han, M., Gao, X., Su, J.Z. & Nie, S. *Nat. Biotechnol.* **19**, 631-635 (2001).
5. Zhao, X., Tapec-Dytioco, R. & Tan, W. *J. Am. Chem. Soc.* **125**, 11474-11475 (2003).
6. Nam, J.-M., Thaxton, C.S. & Mirkin, C.A. *Science* **301**, 1884-1886 (2003).
7. Swierczewska, M., Liu, G., Lee, S. & Chen, X. *Chem. Soc. Rev.* **41**, 2641-2655 (2012).
8. Hindson, C.M., Chevillet, J.R., Briggs, H.A., Gallichotte, E.N., Ruf, I.K., Hindson, B.J., Vessella, R.L. & Tewari, M. *Nat. Methods* **10**, 1003-1005 (2013).
9. Gerasimova, Y.V. & Kolpashchikov, D.M. *Chem. Soc. Rev.* **43**, 6405-6438 (2014).
10. Duan, R., Lou, X. & Xia, F. *Chem. Soc. Rev.* **45**, 1738-1749 (2016).
11. Hughes, T., Janssen, J., Morgan, G., Martiat, P., Saglio, G., Pignon, J., Pignatti, F., Mills, K., Keating, A. & Gluckman, E. *Lancet* **335**, 1037-1038 (1990).

12. Colomb, W. & Sarkar, S.K. *Phys. Life Rev.* **13**, 107-137 (2015).

13. Sheehan, P.E. & Whitman, L.J. *Nano Lett.* **5**, 803-807 (2005).

14. Holzmeister, P., Acuna, G.P., Grohmann, D. & Tinnefeld, P. *Chem. Soc. Rev.* **43**, 1014-1028 (2014).

15. Walter, N.G., Huang, C.-Y., Manzo, A.J. & Sobhy, M.A. *Nat. Methods* **5**, 475-489 (2008).

16. Jungmann, R., Steinhauer, C., Scheible, M., Kuzyk, A., Tinnefeld, P. & Simmel, F.C. *Nano Lett.* **10**, 4756-4761 (2010).

17. Ayala-Orozco, C., Liu, J.G., Knight, M.W., Wang, Y., Day, J.K., Nordlander, P. & Halas, N.J. *Nano Lett.* **14**, 2926-2933 (2014).

18. Johnson-Buck, A., Su, X., Giraldez, M.D., Zhao, M., Tewari, M. & Walter, N.G. *Nat. Biotechnol.* **33**, 730-732 (2015).

19. Nieuwenhuizen, R.P., Bates, M., Szymborska, A., Lidke, K.A., Rieger, B. & Stallinga, S. *PloS one* **10**, e0127989 (2015).

20. Jungmann, R., Avendaño, M.S., Dai, M., Woehrstein, J.B., Agasti, S.S., Feiger, Z., Rodal, A. & Yin, P. *Nat. Methods* (2016).

21. Nam, J.-M., Oh, J.-W., Lee, H. & Suh, Y.D. *Acc. Chem. Res.* **49**, 2746-2755 (2016).

22. Kumar, A., Kim, S. & Nam, J.-M. *J. Am. Chem. Soc.* **138**, 14509-14525 (2016).

23. Lee, Y.K., Kim, S., Oh, J.W. & Nam, J.M. *J. Am. Chem. Soc.* **136**, 4081-4088 (2014).

24. Zhang, D.Y., Chen, S.X. & Yin, P. *Nat. Chem.* **4**, 208-214 (2012).

25. Ouldridge, T.E., Šulc, P., Romano, F., Doye, J.P. & Louis, A.A.

Nucleic Acids Res. **41**, 8886-8895 (2013).

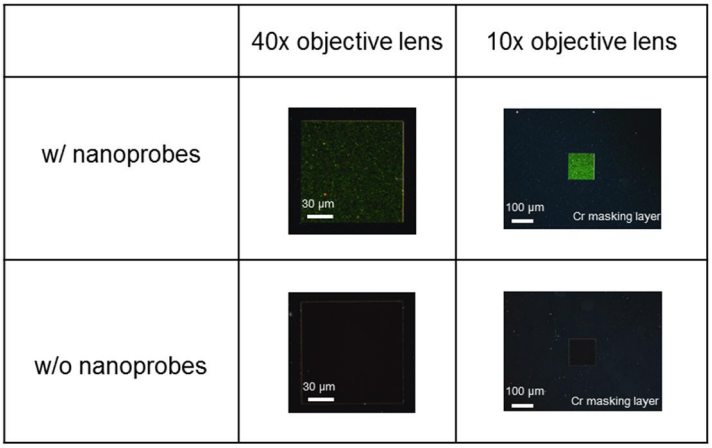

Figure 2.1. Optimization of streptavidin (STV) amount to minimize the nonspecific binding of nanoprobes on the Cr surface of a micropatterned SLB. Dark-field images (zoom-in and zoom-out images) of STV-conjugated SLB micropattern with (top) and without (bottom) the conjugation of nanoprobes. Biotin-functionalized DNA-modified AuNPs were confined within the STV-conjugated SLB pattern area with minimal nonspecific binding of nanoprobes outside the SLB micropattern. The SLB was selectively formed on the glass-exposed square area enclosed by the Cr masking pattern. BSA was used as a blocking agent.

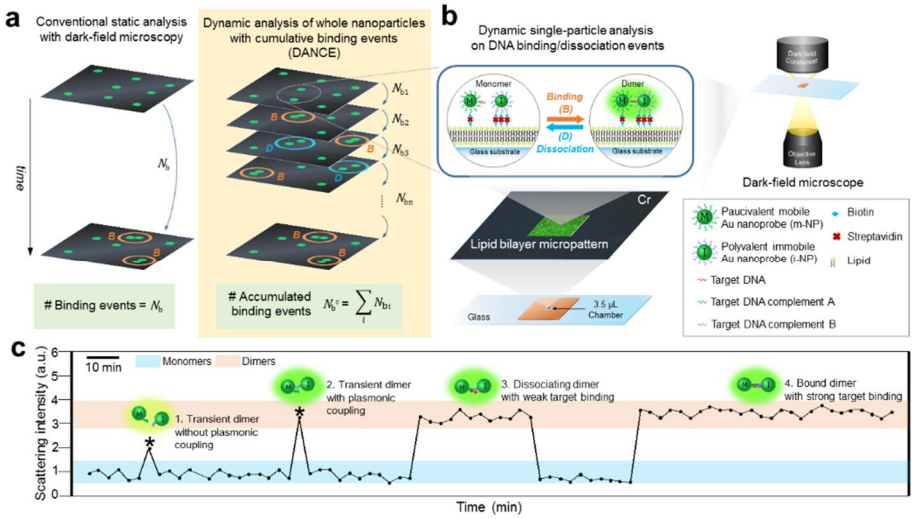

Figure 2.2. Dynamic analysis on whole nanoparticle cumulative binding events (DANCE) with nanoparticle-modified lipid bilayer micropatterns (NLMs). (**a**) Schematic comparison of conventional static analysis and real-time DANCE with dark-field microscopy. (**b**) Single-particle-level analysis on dynamic DNA binding/dissociation events with mobile and immobile plasmonic nanoprobes on lipid bilayer micropattern. (**c**) Time-dependent dark-field scattering signal changes for different dynamic binding modes of DNA-modified plasmonic nanoparticles.

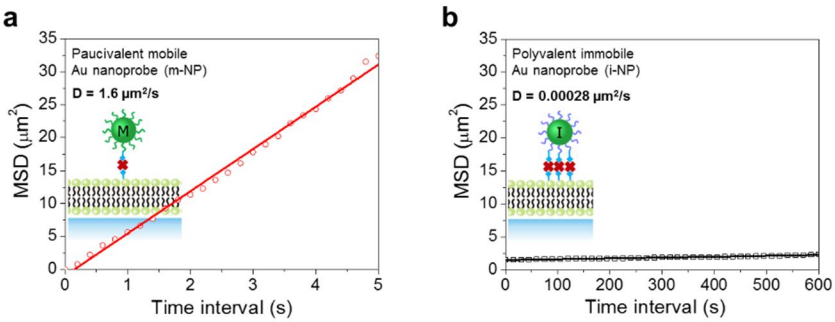

Figure 2.3. Representative mean square displacements (MSDs) of paucivalent mobile Au nanoprobes (m-NPs) (**a**) and polyvalent immobile Au nanoprobes (i-NPs) (**b**) as a function of time interval. Linear relationship between MSD and time interval demonstrates the random 2D Brownian motions of nanoprobes. The diffusion coefficients (D) of m-NPs and i-NPs were estimated to be 1.6 $\mu m^2/s$ and 2.8×10^{-4} $\mu m^2/s$, respectively.

$$\mathrm{MSD}(\Delta t) = < (\boldsymbol{x_{i+n}} - \boldsymbol{x_i})^2 + (\boldsymbol{y_{i+n}} - \boldsymbol{y_i})^2 >$$

$$\mathrm{n} = 1, 2, 3, \ldots, (N_T - 1)$$

$$\mathrm{MSD}(\Delta t) = 4\,\mathrm{D}t$$

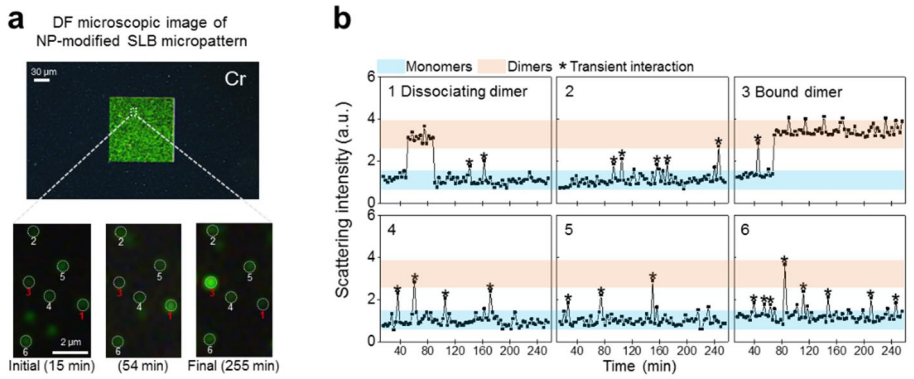

Figure 2.4 Real-time imaging and analysis of DNA binding/dissociating events on NP-modified lipid bilayer micropatterns (NLMs). (**a**) *In situ* dark-field image of nanoprobes on NLM (top). Magnified snapshots of individual nanoprobes at initial (15 min; bottom left), intermediate (54 min; bottom center) and final (255 min; bottom right) states after addition of target DNA and immobile nanoprobes. (**b**) Time-dependent scattering intensity plots with time intervals of 3 min for 6 individual nanoprobes that correspond to the white dotted circles in Figure 2.4a. The blue bands designate the scattering intensity for monomers, and the red bands indicate the dimer scattering intensity. Transient dimeric scatterings of two NPs are marked with an asterisk.

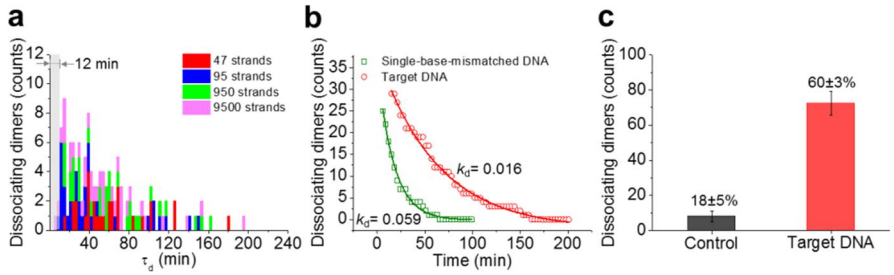

Figure 2.5. (**a**) The time-dependent distribution of the lifetimes of dissociating dimers with varying target DNA amounts (N_{47} = 29, N_{95} = 30, N_{950} = 33, and N_{9500} = 34 dissociating dimers). (**b**) Dissociation kinetics results of the dissociating dimers for perfectly-matched target (5'-GAG GGA TTA TTG TTA AAT ATT GAT AAG GAT-3', 950 DNAs in sample) and single-base-mismatched DNA sequences (5'-GAG GGA TTA TTG TTA AAT ATT GTT AAG GAT-3', 950 DNAs in sample), respectively. The dissociation rate constants of the dissociating dimers with single-base-mismatched DNA and target DNA are 0.059 and 0.016 min^{-1}, respectively. The dissociation half-lives for the dissociating dimers with target DNA and single-base-mismatched DNA are 43.3 min and 11.7 min, respectively. The data are fitted well with the first-order dissociation equation ($y = Aexp(-k_dx) + y_0$) (R^2 = ~0.99 for both cases). (**c**) The comparison of the numbers of dissociating dimers for target DNA sequence and non-complementary sequence.

The numbers above the bars are the percentage of the number of the dissociating dimers in the number of total dimers. All samples contained 200 fM (4.2×10^5 strands) of non-complementary DNA sequence (5'-CTG ATT ACT ATT GCA TCT TCC GTT ACA ACT-3').

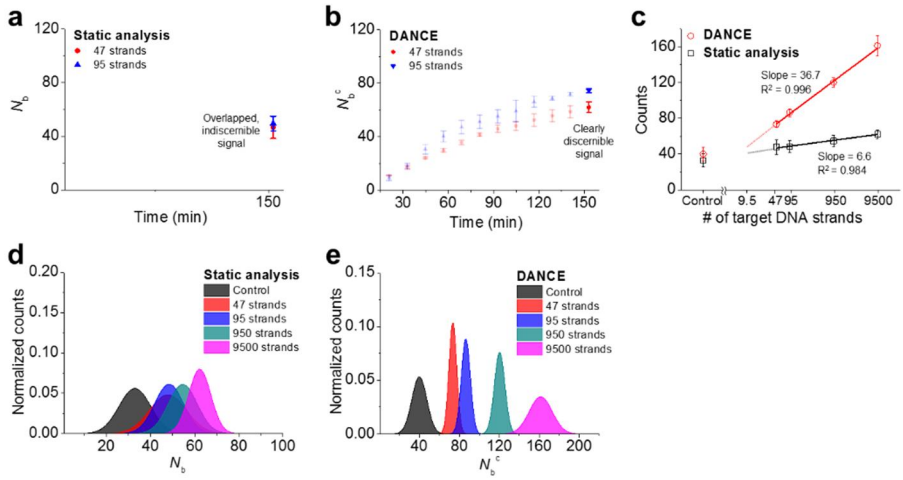

Figure 2.6. Comparisons between static analysis and DANCE on the NLM, quantitative single-base mismatch analysis, and human serum assay results. (**a**) Static analysis with overlapped, indiscernible signals between 47 and 95 target DNA cases after 153 min incubation. (**b**) DANCE results (12 min interval) with clearly discernible signals between 47 and 95 target DNA cases after 153 min incubation. (**c**) Comparison between quantitative DANCE (N_b^c) and static analysis results (N_b). The slope of the DANCE graph line is ~5.6 times steeper than that of the static analysis graph line. The normal distribution curves for the numbers of binding events (N_b) (**d**) and the numbers of cumulative binding events (N_b^c) (**e**) with control DNA, 47, 95, 950, and 9,500 target DNA strands (4 h; 12 min interval). Normal distribution curves are determined from a Gaussian function with mean value and standard deviation at 4 h.

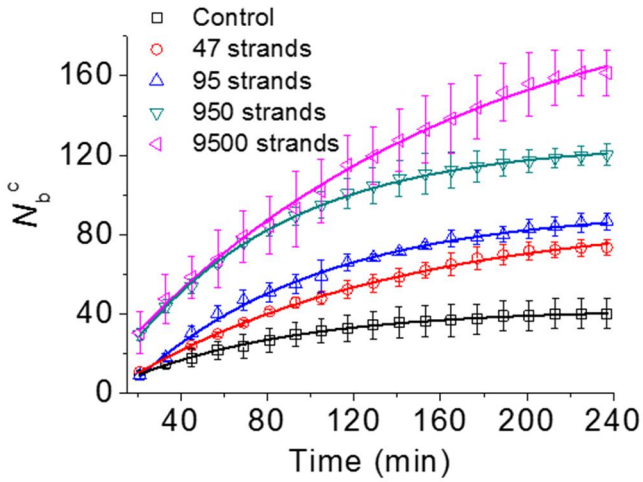

Figure 2.7. Kinetics plot shows sensitivity and reproducibility of detection of DNA strands by DANCE. Binding kinetics plot of cumulative binding events (N_b^c) with different concentrations of target DNA.

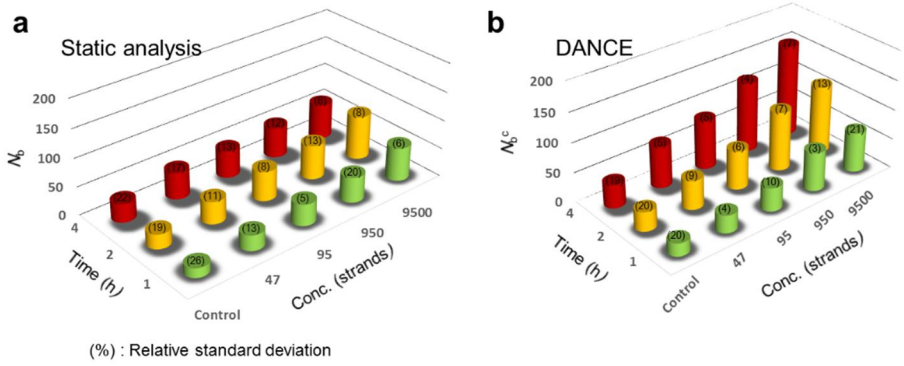

Figure 2.8. Comparison between static analysis and DANCE by variables of concentration and observation time. (a) Using the static analysis, direct correlation among N_b, concentration of nucleic acids, and observation time appears to be weak. (b) Using DANCE method, the correlation among N_b^c, concentration of nucleic acid and observation time is clearly shown.

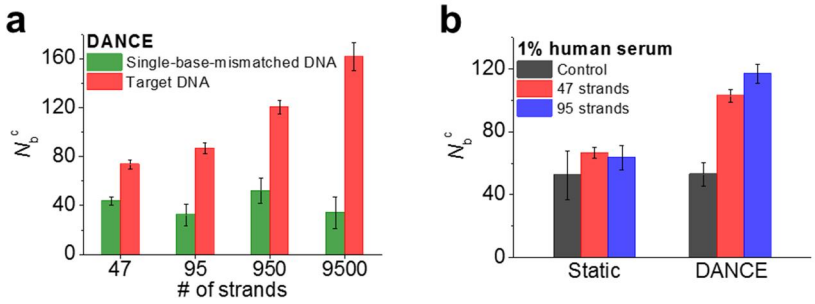

Figure 2.9. (a) DNA concentration-dependent target DNA and single-base-mismatched DNA detection experimental results. (b) Human serum assay results with control, 47 and 95 target DNA strands in samples (153 min incubation). All samples contained 200 fM (4.2×10^5 strands) of non-complementary DNA strands. The error bars were obtained based on four independent experiments with 6,161 ± 462 m-NPs and 1,938 ± 257 i-NPs on each batch of SLB micropatterns.

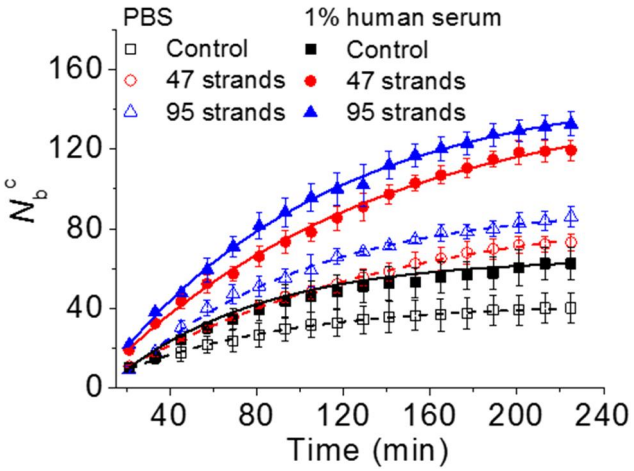

Figure 2.10. Reaction kinetics plots of N_b^c versus time with control, 47 and 95 DNA strands in PBS and 1% human serum. Reactions in PBS are indicated by open symbols and those in 1% human serum are indicated by filled symbols.

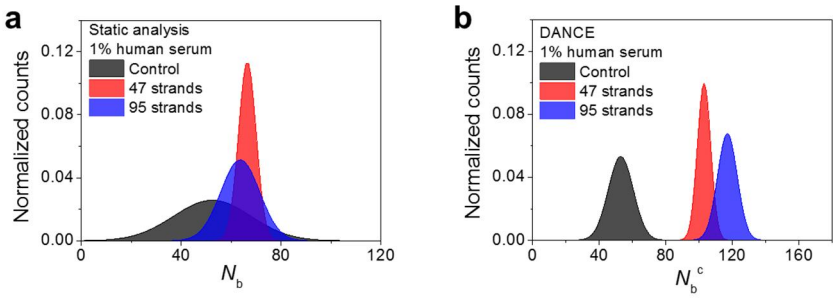

Figure 2.11. Target sensitivities calculated by normal distribution curve with an average and standard deviation using static analysis and DANCE in 1% human serum. (a) Conventional static analysis produces overlapping, indiscernible signals between control and 47 and 95 strands of target DNA after 153 min. (**b**) DANCE, via hybridization of target DNA through snapshots as regular time intervals, is able to discriminate between control and 47 strands of DNA after 153 min, as shown by clearly discernable signals. The sensitivity to differentiate between 47 and 95 strands of target is 89.6%.

Chapter 3

The Stability of Single DNA Duplex Monitored on Dissociating Nanodimer Analysis

3.1. Introduction

After the Human Genome Project was successfully accomplished[1-4], the fast and accurate DNA sequencing and sensing technology is needed. The single nucleotide polymorphism (SNP) is revealed as a common genetic variation among individuals at least 1% population. SNPs can also occur once in every 1000 nucleotides on average in an individual genome, which means that 3-5 million SNPs are contained in the human genome.[5] Most SNPs do not affect the cellular function; however, some SNPs are related to the cause of genetic disease such as cancer. Accordingly, the accurate detection of single base mismatched sequences can play an important role to the development of clinical application such as an early diagnosis of genetic disease. In addition, single nucleotide mutation detection can have an influence to fabricate exquisite DNA-based nanoassemblies (e.g. DNA origami) and toehold DNA switch-based molecular circuits or logic gates.

Over the last decade, a number of SNP detection methods have been developed with various technologies[6-8]. Enzyme-based methods such as primer extension[9-12], microarrays[13, 14], oligonucleotide ligation[15-17], and endonuclease cleavage[18-20] have presented prominent and attractive results, however, enzyme-based methods require time-consuming process with expensive and chemically unstable reagents. Hybridization-based detection methods such as DNA melting analysis[21, 22], dynamic allele-specific hybridization (DASH)[23-25], molecular beacons[26-29], barcode assays[30, 31], and hybridization chain reactions[32-34] provide an alternative to discriminate target

sequences from single base mismatched (SBM) sequences. In particular, the state-of-the-art single molecule fluorescence techniques enable to surpass the limitation of conventional methods owing to the high specificity and sensitivity at the single-molecule level without additional enzyme[35, 36]. With the aid of those cutting-edge technologies, hybridization methods can be improved by fluorescence-based methods such as situ hybridization (FISH)[37, 38], flow cytometry[39, 40], and fluorescence microscopy[41]. However, most experiments about the discrimination of the perfect matched sequences from SBM sequences employed single point mutations at the middle position as representative SBM sequences because single nucleotide variant sequences at the middle position can allow the highest selectivity with perfect matched sequence, due to the formation of the most unstable duplex. The accurate detection and discrimination of single base mismatched strands is still challenging, in particular, and the mutant position-dependent kinetic landscape has not thoroughly explored yet.

Fundamental study of nucleic acid hybridization (i.e annealing process) and dehybridization (i.e. melting process) have an impact on not only deep understanding of fundamental biophysical informations such as detail kinetic feature during duplex formation, the gene regulatory system related to toehold switches, and specific DNA-protein interaction but also various applications such as ultrasensitve DNA or RNA sensors, gene (e.g. miRNA and siRNA) delivery-based therapeutic system, and DNA-origami based nanotechnology. In the 'zip-up' model,[42, 43] DNA hybridization proceeds first through a slow

nucleation step and then through a zipping step. For this nucleation step in the zip-up model, 2 or 3 bp matching should be enough to proceed through next step because of negative effective activation enthalpies.[43, 44] However, T. Ha group supported further the requirement of 7 contiguous Watson-Crick base pairs for quick hybridization of two oligonucleotides.[45] They used single-molecule porous-vesicle encapsulation assay. This method was based on single-molecule Föster resonance energy transfer (FRET)[46] that can visualize the multiple annealing and melting reactions for a pair of DNA or RNA strands freely diffusing inside a porous vesicle. However, the observation of exact kinetic behavior of nucleic acids at the single molecule level and the precise interpretation of association and dissociation of DNA strands remains challenging. To investigate single mutant position-dependent kinetic feature of SBM oligonucleotides at the single molecule level can also give much information about the understanding of fundamental DNA hybridization reaction and the various applications such as DNA hybridization-based nanoassembly, toehold switch-based logic gate, and SNP-based diagnosis, as previously mentioned. Comparing the association process with the dissociation process in two single stranded sequences (i.e. a target and the complementary sequences), the association process is a bimolecular reaction, and the association rate constant ($\underline{k_{on}}$ or k_a) reveals a simple linear dependence on the concentration of target sequences and less sensitive to the length of oligonucleotide.[47] In contrast, since the dissociation process of DNA duplex is unimolecular reaction, the dissociation reveals a simple exponential decay feature with high sensitivity of target-sequence but no target concentration

dependency. Due to the simplicity and higher sequence specificity, the dissociation rate constant (k_{off} or k_d) would rather be applied to the SBM analysis. However, if the dissociation process is too slow to take hours (e.g. the longer DNA strands case), the fluorescence-based techniques suffer from the inherent photobleaching and photoblinking.

Until now, most single molecule studies have been performed using fluorescence-based techniques (e.g. FRET) using very expensive and complexed equipment such as total internal reflection fluorescence (TIRF) system with high power laser light source and highly sensitive CCD. Additionally, the observation time with fluorescence microscope is limited due to the generation of unwanted signals such as time-dependent photobleaching and photoblinking of fluorescent molecules. Such a fluorescence-based system with disadvantages can be replaced by the dark-field light scattering system with plasmonic nanoparticles. Plasmonic nanoparticles can generate strong and stable scattering signal without photobleaching and photoblinking enough for the measurement at single particle level, even by the white light illuminated from a tungsten lamp. Because the plasmonic coupling occurs in the range of several nm, this system can be used in the measurement of binding reaction of biomolecules such as DNA hybridization. Even on a supported lipid bilayer platform, the dynamic DNA reaction can be monitored by DNA-immobilized plasmonic nanoparticels with a dark-field microscope.

Here, we used dark-field scattering signal changes from plasmonic

nanoprobes on a supported lipid bilayer (SLB) micropattern for in-situ monitoring of single target DNA dissociation behavior with the mutant position dependency of SBM sequences.

3.2. Experimental Section

Materials: 1,2-dioleoyl-sn-glycero-3-phosphocholine (DOPC), 1,2-dioleoyl-sn-glycero-3-phosphoethanolamine-N-[methoxy(polyethylene glycol)-1000] (mPEG1k-DOPE), and 1,2-di-(9Z-octadecenoyl)-sn-glycero-3-phosphoethanolamine-N-(cap biotinyl) (biotinylated DOPE) were obtained from Avanti Polar Lipids (Alabaster, AL). Streptavidin was purchased from Molecular Probes (Eugene, OR). Pure streptavidin and bovine serum albumin (BSA) were purchased from Sigma-Aldrich (St. Louis, MO). Phosphate-buffered saline (PBS) solution was prepared by dissolving a PBS tablet (Sigma-Aldrich, St. Louis, MO) in 200 mL DI water, yielding 10 mm phosphate buffer solution with 2.7 mm potassium chloride and 137 mm sodium chloride (pH 7.4). Nanopure water with the minimum resistance (>18 MΩ cm^{-1}) was used in all the experiments. For vesicle preparation (vesicle extrusion), polycarbonate (PC) filters (Whatman, Fisher Scientific) with a pore diameter of 100 nm were used. Fisherfinest premium cover glass (Fisher Scientific) was employed as a support for the lipid bilayer. Organic solvents such as chloroform, acetone and ethanol were obtained from Duksan Pure Chemicals Co. Ltd. (Kyeongi-do, South Korea). Sulfuric acid and hydrogen peroxide were purchased from Daejung Chemicals & Metals Co. Ltd. (Kyeongi-do, South Korea).

Formation of Supported Lipid Bilayers: All the reactions are conducted on a 120 × 120 μm^2 patterned chrome film on a cover glass fabricated by conventional photolithography followed by a lift-off process. SLB was

formed on a bottom glass substrate by the fusion of small unilamellar vesicles (SUVs). SUVs that are used in protein-sensing applications contain 97.1 mol% of DOPC, 2.5 mol% of mPEG1k-DOPE, and 0.4 mol% of biotinylated DOPE. The SUV solution was prepared by dissolving the appropriate amounts of lipids in chloroform. The lipid solution was evaporated in a 50 mL round-bottomed flask using a rotary evaporator at room temperature, under vacuum, for 1 h. The dried mixture was resuspended in DI water and subjected to repeated freeze-thaw cycles at least three times. The total lipid concentration was 2 mg mL^{-1}. The solution was extruded more than 21 times through a PC membrane with a pore diameter of 100 nm at 25 °C. The resulting SUV solution was mixed 1:1 v/v with PBS. The diluted solution (～50 μL) was injected to the flow chamber. After 30 min of incubation at 25 °C, excess and unfused SUVs were eliminated by introducing continuous DIW flows.

Tethering gold nanoparticles to supported lipid bilayers: For tethering of DNA-modified gold nanoparticles, STV and biotin interaction is employed. First 60 nM STV in PBS was incubated with biotin-functionalized supported lipid membrane for 1h at room temperature. Unbound excess STV was washed with copious amounts of PBS. And 10 pM of DNA-modified gold nanoparticles was incubated for 10 min in 25 mM PBS. 1 μM of biotin-containing PB was introduced to remove access unbound gold nanoparticles and quench unreacted binding site of STV. After 15 min, buffer was replaced with PBS for the next reactions.

3.3. Results and Discussion

As the schematic illustration of this study is presented in Fig. 3.1, the binding and dissociation reactions of a single target DNA strands was monitored by the dark-field scattering signal of complementary DNA-modified plasmonic nanoprobes on a fluidic lipid bilayer micropattern. This observation system was the same as the ADNA platform described in detail in Chapter 2. In order to realize a single molecule correlated binding dynamics, only 950 copies of target DNA sequences were added to 6,000~8,000 m-NPs tethered on SLB micropattern, followed by adding i-NPs; 2,000~3,000 i-NPs were finally immobilized on a SLB micropattern. Dynamic binding and dissociation reaction between m-NPs and i-NPs on the 2D fluidic can be efficiently monitoring by the observation of the scattering signal change at the i-NPs fixed point. As we mentioned before, the dissociation kinetics of DNA duplex is simple, more sequence-specific and advantageous to the SBM detection, so that we focus on the dissociation reaction rather than the association reaction to analyze mutant position-dependent SBM kinetics.

To obtain the mutant position-dependent kinetic information of various SBM sequences, we employed the three DNA hybridization system, as shown in Fig.3.1a. 15 mer sequence of a 30 mer perfect matched or a SBM sequence was fixed as the invariable sequence (corresponding to right 15 mer segment of red colored 30 mer strand in Fig. 3.1a), which was hybridized with a complementary sequence immobilized on a m-NP. The other 15 mer sequence

of 30 mer target was the variable sequence with mutant-position, which was hybridized with a complementary sequence immobilized on an i-NP.

When we monitored a single DNA mediated NP dynamic association and dissociation by a dark-field microscope, firstly, a dim green light spot of i-NP changed to a bright green colored spot, which is attributed to the formation of dimeric structure with an i-NP and an m-NP on SLB micropattern. The dimeric scattering intensity is larger than the sum of scattering intensities with two 50 nm AuNP monomers due to the plasmonic coupling with narrow gap between NPs via DNA hybridization, as shown in Fig. 3.1c. From the time-resolved scattering intensity profile at a single i-NP, we can obtain the information of dissociation kinetics for a target DNA at the single molecule level; τ_{on} residence time is correlated not with the association kinetics but to the dissociation kinetics.

Before the mutant position-dependent kinetics of SBM sequences was investigated, we firstly examined the effect of base-pairing length for the dissociation kinetics of perfect matched sequences. For analyzing the length effect of target sequence, the target sequences were varied with 30, 28, 24, 23, 22, and 21 mer strands (Fig. 3.2a). While the fixed one segment (15 mer) of a target sequence hybridized with the complementary sequence on m-NP, the other freely extended segment of a target sequence was gradually reduced from 15 mer to 6 mer. To find the k_{off} value of various sequences respectively, we arbitrarily chose and analyzed 30 dissociating nanodimers of whole nanodimers on a lipid micropattern for the fitting of dissociation profile with

τ_{on} values. As shown in Fig 3.2b, the dissociation reactions of all the sequences respectively were well matched with the simple exponential decay process. With the shorter duplex sequence, as expected, the averaged k_{off} value is gradually increased, which means that the duplex becomes unstable (Fig. 3.2c). Interestingly, the k_{off} values for 6 mer extended target sequence jumped over from 0.232 to 0.358 with 54 % increase compared to 7mer extended sequence. Such significant instability from 6mer extended sequence seems to be related to the seven contiguous Watson-Crick base pair rule.[45]

To investigate the stability of the duplex according to the position of single-base mismatch in short sequence, we fixed freely extended variable bases as seven bases which is hybridized with the complementary sequence of i-NP. As shown in Fig. 3.3, single mismatched sequence was completely discriminated from the target sequence regardless of mismatch position by ADNA system. When a mismatch sequence is positioned at the center of target sequence, i.e. 7 mer-4, the averaged k_{off} value (0.537) exhibits 2.3 times larger than perfect matched target and the highest value compared to those of other single mismatched sequences.

For a longer target sequence (i.e. 15 mer), the k_{off} can be measured according to the mismatch position (Fig. 3.4). As the mismatched base-pair is positioned toward the terminus of complementary sequence on i-NP (i.e. both proximal and distal ends of complementary sequence immobilized on i-NP surface), k_{off} gradually decreases. It means that the single mismatched variance at terminus position has a less significant effect to destabilize duplex strands compared to

the middle position, as previously mentioned. However, for 15mer target sequence, the k_{off} of the middle mismatch (i.e. 15 mer-8) was unexpectedly reduced compared to those of both neighboring mismatches (15 mer-7 and 15 mer-9) (Fig 3.4c). This result is the opposite of the trend in the duplex with 7mer extended target sequence, as described before. A closer look at the middle mismatch sequence, 15 mer-8 reveals that two fairly stable 7 contiguous base pairs were positioned both sides from the middle mismatch point. In contrast, both 15 mer-7 and 15 mer-9 have an unstable 6 contiguous base pairs and a stable 8 contiguous base pairs. Therefore, based on the seven base pair stabilizing model, it is presumed that this unusual trend of k_{off} is due to the stabilization energy by both seven base pairs in 15 mer-8 larger than a sum of stabilization energy by 8 contiguous base pairs and destabilization energy by 6 contiguous base pairs in both 15 mer-7 and 15 mer-9.

To verify if the unusual stability of 15 mer-8 is attributed to seven contiguous base pairing stabilization model, we introduced 13 mer extended target sequence, bearing two 6 contiguous base pairs at both sides from the middle point of the extended sequence (Fig. 3.5). Even though 13 mer extended target sequence is only 2 bp shorter than 15mer extended target sequence, the trend of k_{off} was shown to be reversed as compared to middle mismatch zone of 15 mer. For 13 mer extended target sequence, both two unstable 6 contiguous base pairs in a 13 mer-7 strand destabilize the duplex strands with single mismatch nucleotide at a middle position, and thus the stability of 13 mer-7 is

less stable than both 13 mer-6 and 13 mer-8 bearing a stable 7 contiguous base pair.

As a further test of the apparent requirement of seven contiguous base pairs for stabilizing the duplex, we compared with dissociation rate constants of various sequences in length with matched 6 contiguous base pairs at one side (Fig. 3.6). Interestingly, the k_{off} values for 15 mer-9 with only stable 8 contiguous base pairs sharply decreased from 0.358 to 0.103 with 2.48 times decline compared to 6 mer extended sequence, which 15 mer-9 is more stable. Moreover, as compared with dissociation rate constants of various sequences in length with matched 7 contiguous base pairs at one side (Fig. 3.7), we provided meaning of the other side in the stability of the duplex.

3.4. Conclusion

Mutant position determination of single base mismatched (SBM) DNA sequences was successfully achieved. Although the thermodynamic difference among the mutant position-variable SBM sequences is too minuscule to differentiate them, we can measure and analyze the dissociation constants (k_{off}s) of various SBM sequences, respectively, which is obtained by counting dissociating nanodimers on a fluidic lipid bilayer micropattern using dark-field light scattering. As the sequence length is longer, k_{off} value is gradually smaller due to the stability of duplex via multiple Watson-Crick base-pairing; however, the significant reduction of k_{off} value from 6mer to 7mer sequences were exhibited, which seems to be related to the seven contiguous Watson-Crick base pair rule.

In both 7 mer and 13 mer DNA duplex systems, when the mutant position of SBM sequences is located at the middle point, the k_{off} values are the largest, which means the most unstable duplexes. However, in a 15 mer duplex system, unexpectedly the SBM sequence with the middle mutant position (designated as 15 mer-8 sequence) exhibits slightly more stable than both SBM sequences at neighboring positon from the middle position (i.e. 15 mer-7 and 15 mer-9). It can be inferred that such an uncommon stability of 15 mer-8 is attributed to the stability of two seven contiguous base-pairings at both sides from the middle-mismatched position.

Kinetic information of SBM sequences obtained by counting the dissociation events of DNA mediated plasmonic nanodimer, is very sensitive to

discriminate mutant point SBM sequences and helpful to understand the mechanism of DNA hybridization dynamics at the single molecular level. Moreover, our research and platform are expected to give much insight into unveiling the dynamic information of various biological reactions among biomaterials such as nucleic acids, proteins, and carbohydrates and the new biological mechanisms in the cellular level.

3.5. References

1. International_Human_Genome_Sequencing_Consortium *Nature* **409**, 860-921 (2001).
2. Venter, J.C. *et al. Science* **291**, 1304 (2001).
3. Venter, J.C. *Science* **299**, 1183 (2003).
4. Schmutz, J. *et al. Nature* **429**, 365-368 (2004).
5. Shen, W., Tian, Y., Ran, T. & Gao, Z. *TrAC Trends in Analytical Chemistry* **69**, 1-13 (2015).
6. Kim, S. & Misra, A. *Annu Rev Biomed Eng* **9**, 289-320 (2007).
7. Chang, K., Deng, S. & Chen, M. *Biosens. Bioelectron.* **66**, 297-307 (2015).
8. Chen, X. & Sullivan, P.F. *Pharmacogenomics J* **3**, 77-96 (2003).
9. Sokolov, B.P. *Nucleic Acids Res.* **18**, 3671-3671 (1990).
10. Ross, P., Hall, L., Smirnov, I. & Haff, L. *Nat Biotech* **16**, 1347-1351 (1998).
11. Le Hellard, S., Ballereau, S.J., Visscher, P.M., Torrance, H.S., Pinson, J., Morris, S.W., Thomson, M.L., Semple, C.A.M., Muir, W.J., Blackwood, D.H.R., Porteous, D.J. & Evans, K.L. *Nucleic Acids Res.* **30**, e74-e74 (2002).
12. Chang, Y.-M., Ding, S.-T., Lin, E.-C., Wang, L. & Lu, Y.-W. *Sensors and Actuators B: Chemical* **246**, 215-224 (2017).
13. Gunderson, K.L., Steemers, F.J., Lee, G., Mendoza, L.G. & Chee, M.S. *Nat Genet* **37**, 549-554 (2005).
14. Kennedy, G.C. *et al. Nat Biotech* **21**, 1233-1237 (2003).

15. Landegren, U., Kaiser, R., Sanders, J. & Hood, L. *Science* **241**, 1077 (1988).

16. Abravaya, K., Carrino, J.J., Muldoon, S. & Lee, H.H. *Nucleic Acids Res.* **23**, 675-682 (1995).

17. Hardenbol, P. *et al. Genome Research* **15**, 269-275 (2005).

18. Lyamichev, V., Mast, A.L., Hall, J.G., Prudent, J.R., Kaiser, M.W., Takova, T., Kwiatkowski, R.W., Sander, T.J., de Arruda, M., Arco, D.A., Neri, B.P. & Brow, M.A.D. *Nat Biotech* **17**, 292-296 (1999).

19. Hall, J.G., Eis, P.S., Law, S.M., Reynaldo, L.P., Prudent, J.R., Marshall, D.J., Allawi, H.T., Mast, A.L., Dahlberg, J.E., Kwiatkowski, R.W., de Arruda, M., Neri, B.P. & Lyamichev, V.I. *P. Natl. Acad. Sci. U.S.A.* **97**, 8272-8277 (2000).

20. Wang, Q., Yang, C., Xiang, Y., Yuan, R. & Chai, Y. *Biosens. Bioelectron.* **55**, 266-271 (2014).

21. Sorgenfrei, S., Chiu, C.Y., Gonzalez, R.L., Jr., Yu, Y.J., Kim, P., Nuckolls, C. & Shepard, K.L. *Nat Nanotechnol* **6**, 126-132 (2011).

22. Wienken, C.J., Baaske, P., Duhr, S. & Braun, D. *Nucleic Acids Res.* **39**, e52 (2011).

23. Howell, W.M., Jobs, M., Gyllensten, U. & Brookes, A.J. *Nat Biotech* **17**, 87-88 (1999).

24. Germer, S., Holland, M.J. & Higuchi, R. *Genome Research* **10**, 258-266 (2000).

25. Yang, A.H., Hsieh, K., Patterson, A.S., Ferguson, B.S., Eisenstein, M., Plaxco, K.W. & Soh, H.T. *Angew. Chem. Int. Ed.* **53**, 3163-3167

(2014).

26. Tyagi, S., Bratu, D.P. & Kramer, F.R. *Nat Biotech* **16**, 49-53 (1998).

27. Mao, X., Jiang, J., Xu, X., Chu, X., Luo, Y., Shen, G. & Yu, R. *Biosensors and Bioelectronics* **23**, 1555-1561 (2008).

28. Song, S., Liang, Z., Zhang, J., Wang, L., Li, G. & Fan, C. *Angew. Chem. Int. Ed.* **48**, 8670-8674 (2009).

29. Song, Y., Zhang, W., An, Y., Cui, L., Yu, C., Zhu, Z. & Yang, C.J. *Chem Commun (Camb)* **48**, 576-578 (2012).

30. Geiss, G.K. *et al. Nat. Biotechnol.* **26**, 317-325 (2008).

31. Nam, J.-M., Stoeva, S.I. & Mirkin, C.A. *J. Am. Chem. Soc.* **126**, 5932-5933 (2004).

32. Liu, P., Yang, X., Sun, S., Wang, Q., Wang, K., Huang, J., Liu, J. & He, L. *Anal. Chem.* **85**, 7689-7695 (2013).

33. Song, T., Xiao, S., Yao, D., Huang, F., Hu, M. & Liang, H. *Adv. Mater.* **26**, 6181-6185 (2014).

34. Qing, Z., He, X., Huang, J., Wang, K., Zou, Z., Qing, T., Mao, Z., Shi, H. & He, D. *Anal. Chem.* **86**, 4934-4939 (2014).

35. Miotke, L., Barducci, M. & Astakhova, K. *Chemosensors* **3**, 224-240 (2015).

36. Gaspar, I. & Ephrussi, A. *Wiley Interdiscip Rev Dev Biol* **4**, 135-150 (2015).

37. Raj, A., van den Bogaard, P., Rifkin, S.A., van Oudenaarden, A. & Tyagi, S. *Nat Meth* **5**, 877-879 (2008).

38. Amann, R. & Fuchs, B.M. *Nat Rev Microbiol* **6**, 339-348 (2008).

39. Porichis, F., Hart, M.G., Griesbeck, M., Everett, H.L., Hassan, M., Baxter, A.E., Lindqvist, M., Miller, S.M., Soghoian, D.Z., Kavanagh, D.G., Reynolds, S., Norris, B., Mordecai, S.K., Nguyen, Q., Lai, C. & Kaufmann, D.E. *Nat. Commun.* **5**, 5641 (2014).

40. Baerlocher, G.M., Vulto, I., de Jong, G. & Lansdorp, P.M. *Nat. Protocols* **1**, 2365-2376 (2006).

41. Bystricky, K. *FEBS Lett* **589**, 3014-3022 (2015).

42. Pörschke, D. & Eigen, M. *Journal of molecular biology* **62**, 361IN11365-11364IN15381 (1971).

43. Ouldridge, T.E., Šulc, P., Romano, F., Doye, J.P. & Louis, A.A. *Nucleic Acids Res.* **41**, 8886-8895 (2013).

44. Schreck, J.S., Ouldridge, T.E., Romano, F., Šulc, P., Shaw, L.P., Louis, A.A. & Doye, J.P. *Nucleic Acids Res.* **43**, 6181-6190 (2015).

45. Cisse, I.I., Kim, H. & Ha, T. *Nat. Struct. Mol. Biol.* **19**, 623-627 (2012).

46. Ha, T., Enderle, T., Ogletree, D., Chemla, D.S., Selvin, P.R. & Weiss, S. *P. Natl. Acad. Sci. U.S.A.* **93**, 6264-6268 (1996).

47. Dupuis, N.F., Holmstrom, E.D. & Nesbitt, D.J. *Biophys. J.* **105**, 756-766 (2013).

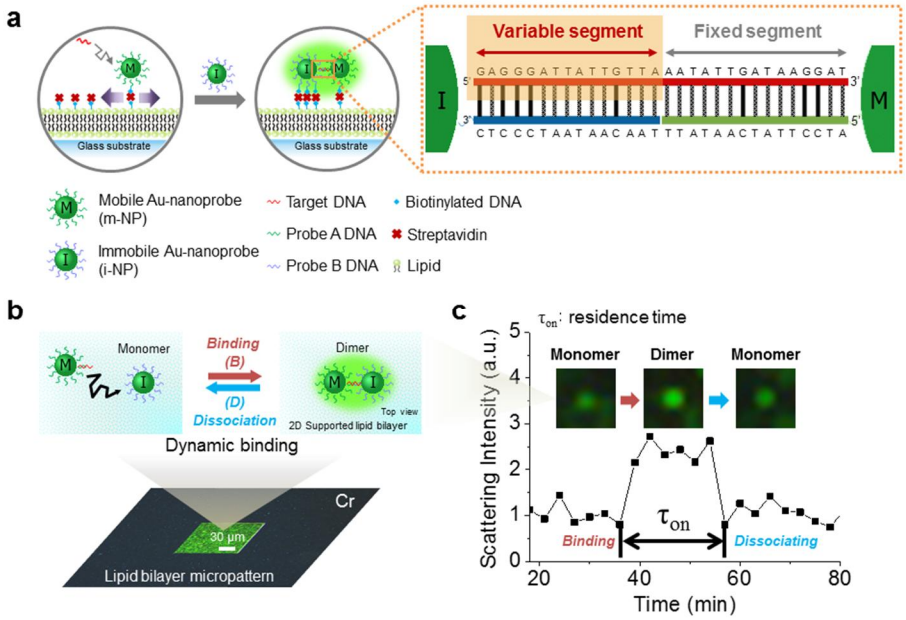

Figure 3.1. Schematic illustration of point-mutation determination with mutant position at the single molecule level. (a) (Left) Target DNA detection using DNA modified Au nanoprobes on supported lipid bilayer. (Right) Target sequence with variable segment (for point-mutation) and fixed segment. (b) Dark-field scattering-based in-situ monitoring of plasmonic nanoparticles dynamic binding reaction. (c) Kinetic profile of a dissociating nanodimer via a single DNA hybridization by dark-field scattering analysis.

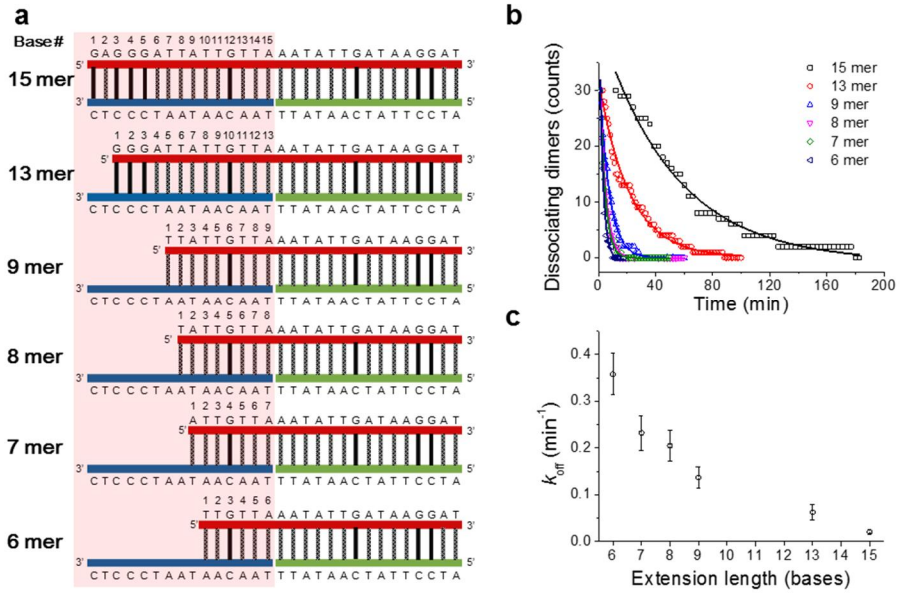

Figure 3.2. Sequence length-dependent dissociation feature. (a) Duplex forms between target sequences with different lengths and the complementary sequences. (b) Dissociating feature of dissociating nanodimers with target lengths. (c) Averaged k_{off} values according to extended DNA lengths.

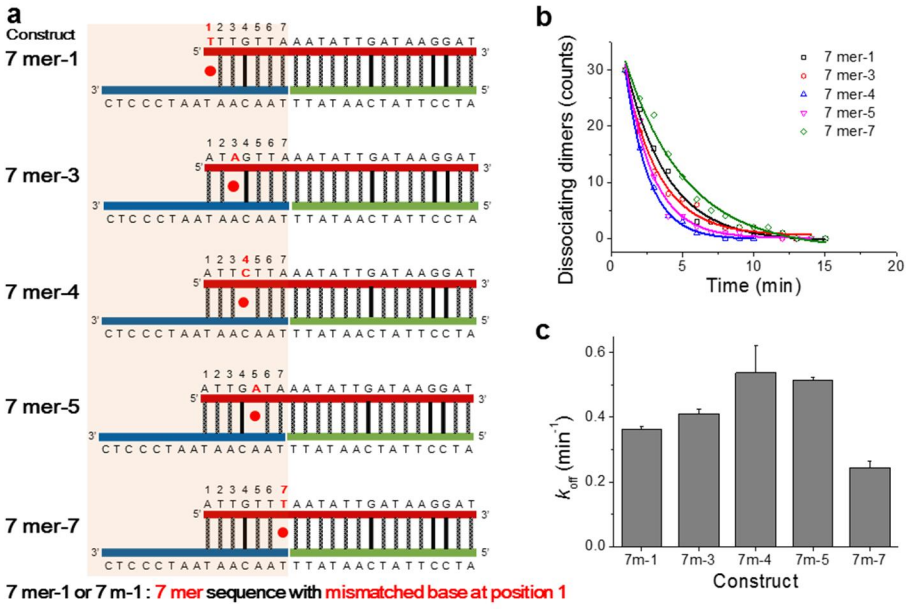

Figure 3.3. Mutant position-dependent dissociation feature in seven base pairings. (a) Duplex forms between point-mutation seven base paring sequences with different position and the complementary sequences. (b) Dissociating feature of dissociating nanodimers with mutation position. (c) Averaged k_{off} values of point-mutation seven base sequences according to mutation position.

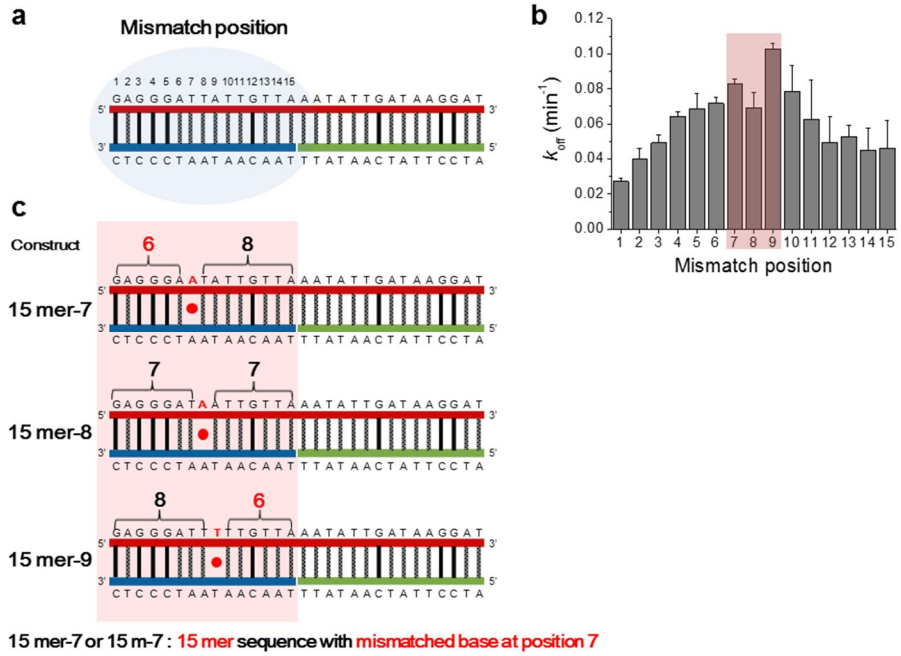

Figure 3.4. The effect of DNA mismatch position on 15 mer variable zone. (a) Mismatch position in fifteen base paring sequence. (b) Averaged k_{off} values of point-mutation fifteen base sequences according to mutation position. (c) Duplex forms between point-mutation fifteen base paring sequences with different position and the complementary sequences.

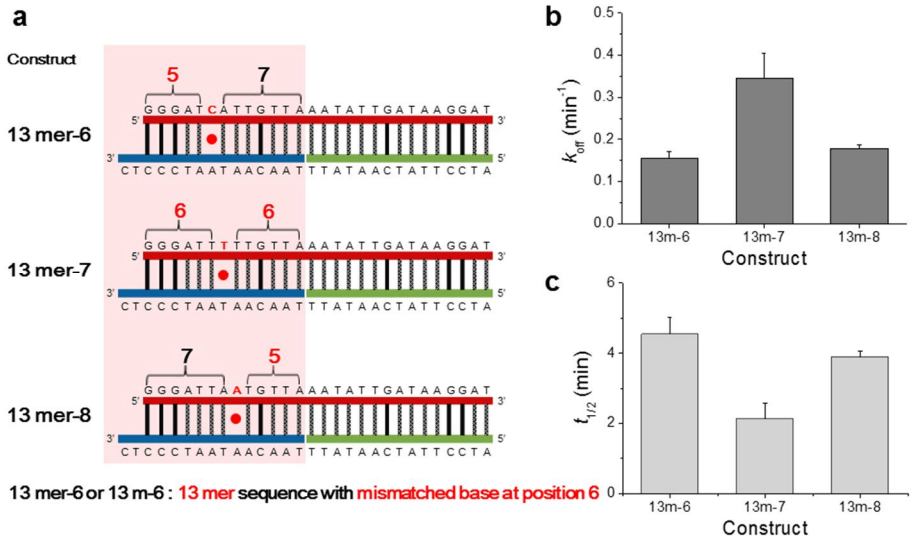

Figure 3.5. The effect of DNA mismatch position on 13 mer variable zone. (a) Duplex forms between point-mutation thirteen base paring sequences with different position and the complementary sequences. (b) Averaged k_{off} values of point-mutation thirteen base sequences according to mutation position. (c) Averaged $t_{1/2}$ values of point-mutation thirteen base sequences according to mutation position.

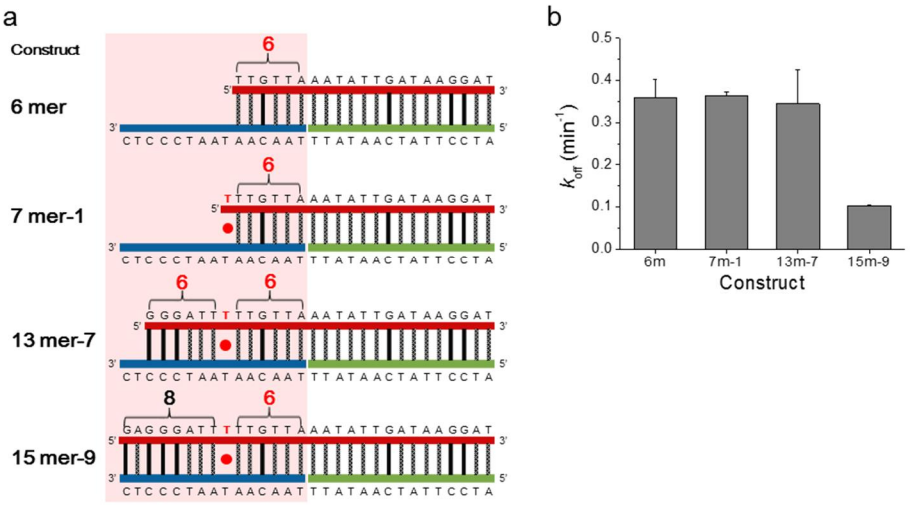

Figure 3.6. Comparing the stability of the duplex with various sequences in length with matched 6 mer base pairs at one side. (a) Duplex forms between various sequences in length with matched 6-mer base pairs at one side and the complementary sequences. (b) Averaged k_{off} values of various point-mutation base sequences.

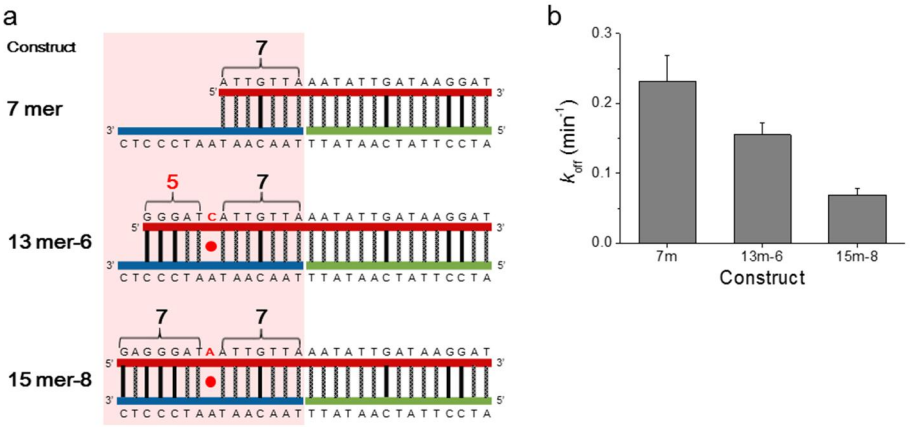

Figure 3.7. Comparing the stability of the duplex with various sequences in length with matched 7 mer base pairs at one side. (a) Duplex forms between various sequences in length with matched 7 mer base pairs at one side and the complementary sequences. (b) Averaged k_{off} values of various point-mutation base sequences.

요약(국문초록)

2차원 유동적 지지형 지질 이중막 마이크로패턴 나노입자 플랫폼을 사용한 DNA 분석

지질 (lipid)은 탄화수소를 포함하는 자연계에 존재하는 물질로서 무극성 용매에 녹으며 지방, 왁스, 스테로이드, 당지질, 인지질 등이 있다. 지질 물질은 유기체에서 에너지를 축적하거나 신호 전달 및 세포막 구조를 구성하는 등 필수적인 역할을 수행하고 있다. 이 중 인지질은 세포막의 주요 구성 지질 분자로서 친수성 머리 그룹과 소수성 꼬리 형태로 구성되어 있는데 이는 자기조립 형태의 이중막 구조를 형성하도록 도와준다 또한 이들은 자리교환을 통해 동적 반응의 연구를 위한 유동성 막 및 세포 모사 모델 막으로 활용되어질 수 있다. 특히, 고체 유리 기판 위에 지지된 지질 이중막 (supported lipid bilayer, SLB)은 생체분자의 반응을 조절시키는 다양한 물리 화학적 기능과 다양한 생체분자들을 지질층 내에 포함시키는 수식 능력 및 광학 장치를 활용하여 동적 반응을 관찰할 수 있게 하는 견고한 플랫폼을 제공한다.

DNA (deoxyribonucleic acid)는 유기체들이 생명을 보존하며 재생산하기 위해 필요한 핵심적인 분자들로서 대를 계승하기 위한 유

전 정보를 포함하고 있는데, 모든 유전 정보들은 DNA 가닥내에 아데닌 (adenine), 시토신 (cytosine), 구아닌 (guanine), 티민 (thymine)의 4종류의 염기로 구성되어 있는 특별한 서열 형태로 암호화 되어 있다. 이러한 DNA 서열은 돌연변이 유도물질에 갑작스럽게 노출되거나 DNA 복제 과정에서 에러가 생기는 것으로 인해 유전자 서열의 변형 즉 무작위의 서열 변형이 일어나는데 이를 통해 유기체들이 대를 이어 갈 때에 유전적인 왜곡이 생기거나 유전체의 기능장애로 인하여 유전병이나 암질환의 발생에 영향을 주게 된다. 지난 수십 년간 DNA 바이오센서는 임상진단, 생물의학 공학, 식품 개발, 환경 보호, 범죄수사 및 생물학전 사전 검사 등의 다양한 분야에 적용할 수 있는 이유로 많은 관심을 받아 왔다. DNA 바이오센서 개발에 주요한 도전 중에 하나가 증폭의 도움 없이 초고감도, 정량분석이 가능한 고신뢰 DNA 검지에 관한 것이다. 효소나 형광 염료 또는 나노물질 등의 사용하여 증폭과정을 거치는 경우 잘못된 신호 및 바탕신호의 증폭까지 동반하여 에러 신호 발생으로 인해 검지에 어려움이 되고 있다. 이런 문제점을 가지고 있는 증폭방법 없이 초고감도의 DNA 검지를 실현하기 위해서는 극저농도의 타겟 DNA로 인해 매우 드물게 발생하는 참 신호의 값을 잘못된 신호로부터 정확하게 분리하는 노력이 필수적이다. 이 논문에서는 플라즈모닉 나노입자를 매단 이차원 유동성 지질 이중막 마이크로패턴 플랫폼을 활

용하였다. 플라즈모닉 나노입자는 고강도의 광산란 신호를 내며 분자결합으로 인하여 발생되는 나노입자들 사이의 수 나노미터 정도의 거리의 변화는 플라즈모닉 커플링을 통해 검지할 수 있다. 게다가 이 플랫폼은 타겟 DNA를 농축할 수 있으며, 이차원 지질 이중막 패턴 내에 결합 반응의 효율을 증가시킬 수 있다. 따라서, 우선 다양한 실험 조건에서 SLB 레이어와 SLB 레이어 위의 나노입자의 특징적인 성질과 기본적인 거동을 연구하였다. 다음에는 초고감도 DNA 센싱을 위해 최적화된 조건을 구하였고, 그것에 더해 이 플랫폼과 방법론을 활용하여 다양한 위치에 각각의 염기서열이 변형된 단일 뉴클레오티드 다변형 서열을 분석하는 데에 적용할 수 있었다.

제 1장에서는 최근에 연구된 나노물질을 지지체로 사용한 이차원 유동성 지지형 지질이중막 구조의 합성법 및 동역학적신호 분석을 통한 바이오센서로서의 응용에 대해서 요약정리 하였다.

제 2장에서는 표면에 DNA로 기능화 된 금나노입자들을 이차원 유동성 지지형 지질 이중막 마이크로패턴에 도입시킨다. 검지하고자 하는 DNA와 금나노입자들 간에 결합 (association or hybridization) 및 분리 (dissociation)의 동역학적 반응은 암시야 현미경 (dark-field microscopy)을 통해 플라즈모닉 나노입자간 산란신호 변화를 측정하였다. 위 동역학적 반응의 분석을 기초로 한 새로운 분석법 (DANCE)을 제안하고 이를 이용 초고감도 (ultrasensitivity)

및 고선택적 (high-selectivity) 바이오센서 플랫폼을 제시하였다.

제 3장에서는 다양한 단일염기변이들 (sinlge base mismatched DNA)을 제 2장의 방법을 이용 나노다이머의 해리상수 (dissociation constants of nanodimers)들을 측정 및 비교하였다. 이를 통해 최소 7개의 염기가 나란히 염기쌍을 형성하여야 안정적 (the seven contiguous Watson-Click base pair rule)임을 주장한 기존의 법칙을 긴 DNA (10-mer 이상)에서도 적용 가능함을 입증 하였다.